TEMPERATURE DEPENDENCE OF THE LA[110] BRILLOUIN SHIFT IN THE STRUCTURAL GLASS : $Rb_{1-X}(NH_4)_XH_2PO_4$

By

ABDELLATIF BOUCHALKHA

Bachelor of Science

Central State University

Edmond, Oklahoma

1986

Submitted to the Faculty of the
Graduate College of the
Oklahoma State University
in partial fulfillment of
the requirements for
the Degree of
MASTER OF SCIENCE
July, 1989

[redacted]

[redacted]

[redacted]

James P. Wilstead

Thesis Adviser

[redacted]

[redacted]

ACKNOWLEDGMENTS

This is a rather important section in this work and I like to start it first by sincerely thanking my thesis adviser Dr. J. P. Wicksted for his advice, guidance, and support throughout this project. I like to acknowledge Dr. G. S. Dixon for his contributions in the crystal growth. I also like to thank him and Dr. S. W. S. McKeever for serving in my thesis committee. Extended thanks go to Mr. G. H. Gangwere with whom I shared all the hard times and good times in the lab. I like to thank him very much for his help and support throughout this work. I also like to thank our collaborators Dr. C. Prieto and Dr. J. Gonzalo at the Universidad Autonoma de Madrid (Spain) for their kindness and hospitality during my visit to their lab.

More importantly, I like to gratefully thank God, my Mom and my Dad for their blessings. Great thanks are also extended to my Sisters, Brothers and friends for their constant support.

Finally, I would like to thank the Physics Department at O.S.U. and especially Dr. P. Westhaus for their help during my first days in Stillwater.

Financial support for this work was provided by a NATO grant under a contract #86/0808 and a University Center for

Energy Research (UCER) grant number 1-1-50780.

TABLE OF CONTENTS

LIST OF TABLES

LIST OF FIGURES

CHAPTER I

INTRODUCTION

Potassium Dihydrogen Phosphate (KDP) is a well known ferroelectric material. It has been under intensive experimental and theoretical investigation ever since its discovery in 1935[1]. The data accumulated through the years is enormous. The interest in this material is mainly due to its piezoelectric and nonlinear properties. Its applications range from the use in World War II submarines to detect pressure waves from nearby enemy submarines, to the more recent applications in controlled fusion reactions namely Inertial Confinement Fusion (ICF)[2]. KDP is also used as a frequency doubler for second harmonic generation of laser light. Today the search is still on for other nonlinear optical materials such as KDP.

Rubidium Dihydrogen Phosphate (RDP) and Ammonium Dihydrogen Phosphate (ADP) are isomorphs of KDP. All of them are in the paraelectric phase at room temperature with a tetragonal point group symmetry $\bar{4}2m$.

RDP undergoes a structural change to a ferroelectric phase with an orthorombic mm2 symmetry at 146 K.The transition is continuous[3] and results from the linear piezoelectric coupling between the soft optic (B2) mode and

an xy-shear acoustic phonon at the zone center. The low temperature spontaneous polarization observed is caused by the relative displacements of the Rb^{+}, P^{5+} and O^{2-} ions in the direction of the c axis.

ADP on the other hand, has a phase transition at 148 K below which it orders antiferroelectrically in an orthorhombic structure with an mmm symmetry. The ordering in this case is due to the formation of H-bonds between the NH_4^+ protons and four nearby PO_4 tetrahedra. This antiferoelectric transition is strongly first order[3], the orthorhombic distortion being that of an M_{34} mode at the zone boundary (M-point).

The mixed crystals of ferroelectric RbH_2PO_4 (RDP) and antiferroelectric $NH_4H_2PO_4$ (ADP) constitute a new family of solid solutions called RADP : $Rb_{1-x}(NH_4)_xH_2PO_4$.

The well known parents, the ease to grow high quality mixed crystals over the whole range of x, the high degree of randomness of the mixtures and the diversity of the experiments that can be performed on these materials have given them a big edge on other contemporary structural glasses. Great interest in these materials developed since the first publication in 1982[4]. In this system of mixed RADP crystals there is a competition between the characteristic ordering of the acid proton in the ferroelectric (FE) phase of RDP and that of the antiferroelectric (AFE) phase of ADP.

Various experiments[5] including the appearance of

domains, birefringence observations, dielectric and X-ray measurements have been performed on these structural glasses. These studies have led to the phase diagram reproduced in Figure 1 [5]. In this diagram one recognizes the PE phase at high temperature for all concentrations as expected, an FE phase for $x \lesssim 0.22$, and an AFE region for $x \gtrsim 0.75$. In the intermediate region where $0.22 \lesssim x \lesssim 0.75$ there is an onset of freezing around T=100 K. This is where the ammonium ions (NH_4^+) start to freeze gradually, suppressing both the FE and AFE transitions and causing the crystal to behave like a glass. This freezing is believed[6] to be due to the NH_4^+ ions forming their own H-bonds with nearby PO_4 tetrahedra, occupying O sites, preventing the FE ordering from occuring.

Recently, some extensive temperature dependent Brillouin scattering studies[7,8] have been done for the concentrations: x=0.25, x=0.35 and x=0.72. Using the strong electrostrictive coupling of the local polarization to acoustic phonons they were able to confirm the existence of an Edwards-Anderson order parameter[9]. Such a parameter is used as an indication of a system forming slow, long range polarization fluctuations as it progresses to a glass-like state.

The current study is designed to grow RADP crystals at new concentrations and perform Brillouin scattering experiments on them. In particular, studies of the longitudinal acoustic phonon propagating in the [110]

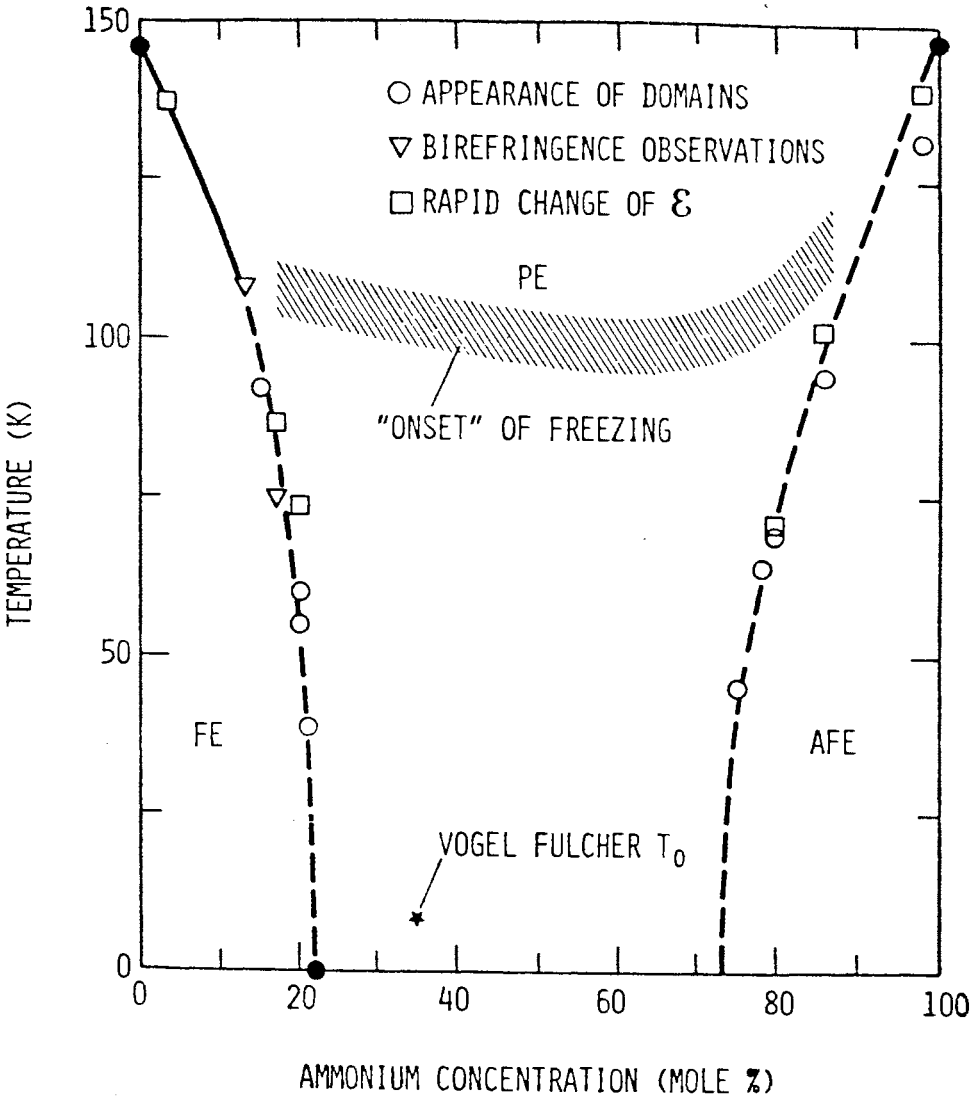

Figure 1. Phase Diagram of RADP Crystals (from Reference 5)

direction (LA[110]) are undertaken as a function of temperature. The goal is to compare the temperature dependence of the LA[110] Brillouin frequency shifts of these new concentrations with those previously studied to determine if the same theoretical analysis can be applied to our results.

CHAPTER II

SAMPLE GROWTH AND PREPARATION

One common way to grow crystals is by separation from aqueous solution. In fact, this is the way most soluble crystals are grown commercially[10]. There are two methods of growth; one is by temperature lowering and the other is by slow evaporation. The latter is the method we used to grow ferroelectric crystals such as KDP, RDP and ADP. The following is a rather brief description of this method.

First, we start out by preparing a saturated water solution of the compound at room temperature. This usually takes 5 to 6 days but this time period can be shortened for certain compounds by raising the temperature of the solution. The longer the solution remains undisturbed the closer it gets to saturation. It is then to our advantage to make an extra quantity of saturated solution for later use (we have to keep some precipitate with the solution to help reach and maintain equilibrium). The next step is to super saturate some of this solution. This is done by warming it 4 to 5°C above room temperature and saturating it again. Once the heating source is off the solution becomes metastable and some nucleation sites will form. Immediately after this, the solution should be placed inside a closed

desiccator which contains a drying agent (i.e. drierite). Now the process is allowed to go on solely with the absorption of the solvent (water) due to the desiccating agent. The nucleation sites that I mentioned earlier, will start to grow and form seeds. This process usually takes a couple days or more depending on what size seeds we want and how viscous the solution is.

Now we are ready to grow crystals. At this stage, we want to try and keep only one nucleation site which is to be the seed. To do that we should filter out the solution from contaminants such as dust particles, etc.

The seeds are now placed in the solution on a round piece of teflon to help the crystal grow from the base as well. Next we slightly warm up the solution to eliminate all unwanted spurious seeds which are either attached to the main seed or floating in the solution. Note that any shaking of the solution is highly likely to trigger other unwanted nucleations. Now we cover the crystallizing dish slightly to adjust the evaporation rate which varies significantly with changes in room temperature, humidity, and crystal specimen. Finally we close the desiccator and hope that after a couple days we will be able to see growth of the seeds. For a good crystal size ($1.5x.5x.3cm^3$), the growing period is about 30 to 40 days. During this period it is very important that the desiccator should not be disturbed in any way.

The crystallographic directions of this family of crystals are shown[11] in Figure 2; they grow longer

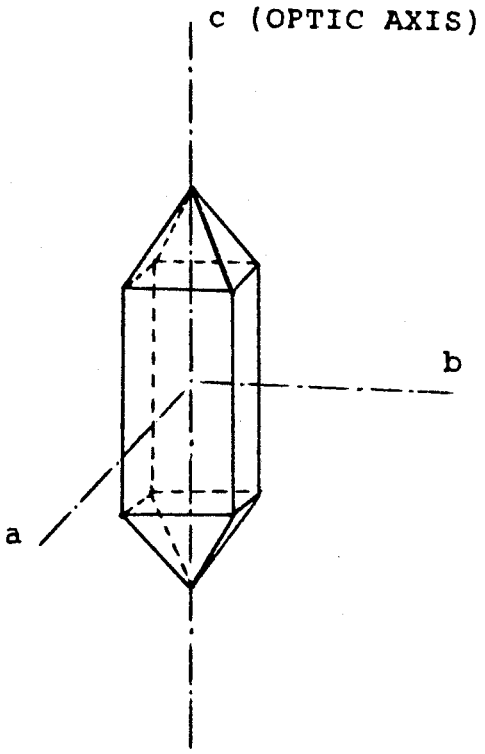

Figure 2. Crystallographic Directions of RADP

along the c-axis (optic axis). ADP, KDP and RDP samples have been grown successfully by this method and used for Brillouin spectroscopy. The results are comparable to what has been published[12].

ADP solutions were prepared as described earlier from chemically pure grade ADP powder[13] dissolved in pure distilled water which was then allowed to saturate. RDP solutions on the other hand were prepared differently since RDP powder was not available commercially. We used Hypophosphoric acid (H_3PO_4), 50% diluted, to neutralize Rubidium Carbonates (Rb_2CO_3)[14]. Saturation occurred when the precipitate started forming. The solution obtained was then filtered and used to grow pure RDP crystals. The RADP mixed crystals were then grown from a mixture of saturated solutions of each component. An estimate of the concentration of the mixed crystal was roughly obtained from the proportions mixed in the solution. Three different solutions with x=0.28, 0.42, 0.48 concentrations were made and a few crystals were grown from each by the same method described earlier. Two samples with x=0.28 and x=0.42 concentrations were selected for this study. Both crystals had similar growth conditions: the crystallizer (or dish holding the solution) volume was 350 ml, the volume of the solution was 100 ml, and the temperature was about (298 ± 3)°K over the growing period of 30 to 40 days.

The samples were polished very carefully using different diamond paste polishing grit and lubricating fluid

(Buehler Metadi Fluid). These crystals were of rather good optical quality except for a few strains suffered during the polishing. Their hygroscopic nature made it necessary to keep them in a closed desiccator free from humidity. After a period of use the samples had to be slightly polished, in order to clean them, since they cannot be treated with acetone or alcohol due to the water contained in these cleaning solutions.

CHAPTER III

THEORY

Brillouin Scattering in General

Brillouin scattering was first discussed by Brillouin in 1914, then published[15] with great detail in 1922. There was not much use for Brillouin scattering back then due to the lack of coherent light sources. It was not until the discovery of lasers[16] in 1960 that Brillouin scattering became a very powerful experimental technique.

In the modern terminology, Brillouin scattering is described as the inelastic scattering of photons from thermally induced density fluctuations or phonons. The light scattered from these propagating acoustic waves is Doppler shifted in frequency giving rise to the Brillouin doublet in the frequency spectrum of the scattered light. The central component called the Rayleigh peak is due to elastic scattering of light by static imperfections and defects in the crystal. The shift in frequency of the Brillouin peaks is very small (on the order of 10^{10} Hz) compared to the unshifted incident light (about 10^{15} Hz). This is due to the fact that the speed of the acoustic phonons (about 10^{5} cm/sec) is much less than the speed of light. A high

resolution instrument, such as the Fabry-Perot interferometer, is necessary to conduct such experiments.

For a given phonon direction of propagation, one obtains a set of dispersion curves (ω vs q)[17] as shown in Figure 3. The graph is always composed of 3s branches where s is the number of atoms per unit cell (s=2 in the case of Figure 3). Three bands called acoustic branches result such that $\omega \rightarrow 0$ as $q \rightarrow 0$. These bands, near q=0, correspond to all atoms in a unit cell moving together and are identical with macroscopic sound waves. The other 3s-3 bands, which will not be considered here, are called optical branches. They correspond to the relative motion of the atoms in a unit cell.

Equations of Motion

We will consider the equations of motion as applied to an elastic medium only. Later on in this chapter we will modify our results to fit a piezoelectric crystal. In the long wavelength limit the equations of motion allow us to determine the elastic constants which in turn determine the polarization and phonon frequencies. Assuming the summation over repeated indices, the equations of motion are written as follows[18]

$$\rho \ddot{u}_i = C_{iklm} \frac{\partial^2 u_m}{\partial r_k \partial r_l} \qquad (3\text{-}1)$$

where $\vec{u}$ is the displacement vector, C_{iklm} are the

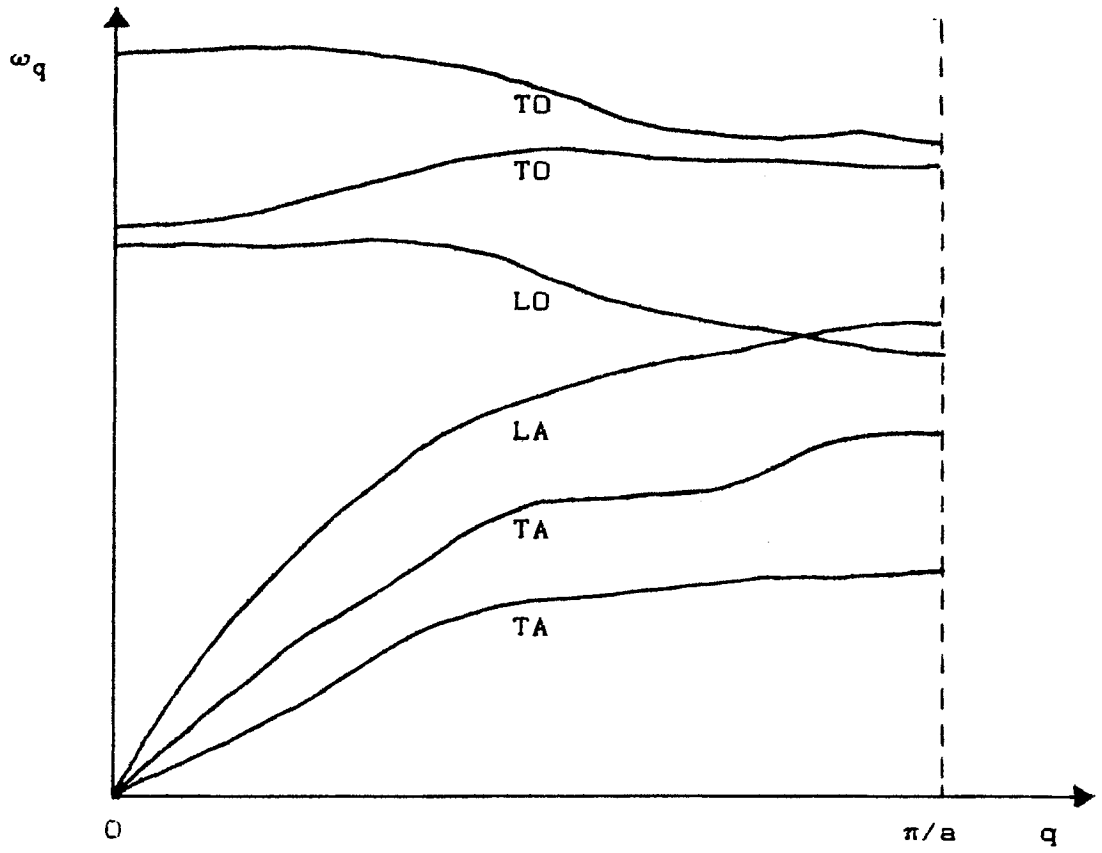

Figure 3. Typical Phonon Dispersion Curves. T and L Stand for Transverse and Longitudinal While O and A Stand for Optic and Acoustic

components of the fourth-rank elastic stiffness tensor and ρ is the density of the material.

Assuming plane wave solutions of the following form :

$$u_m = u_m^o \, e^{i(\vec{q}\cdot\vec{r} - \omega t)} \tag{3-2}$$

and substituting this into Equation (3-1) we get

$$\rho\omega^2 u_i^o = C_{iklm} q_k q_l u_m^o \tag{3-3}$$

or,

$$\left[C_{iklm} q_k q_l - \rho\omega^2 \, \delta_{im}\right] u_m^o = 0 \tag{3-4}$$

q_k and q_l are components of $\vec{q}$.

In the long wavelength approximation we have, $\omega = vq$, where v is the sound velocity. Substituting this into Equation (3-4) we have

$$\left[C_{iklm} \bar{q}_k \bar{q}_l - \rho v^2 \delta_{im}\right] u_m^o = 0 \tag{3-5}$$

where $\bar{q}_k = \frac{q_k}{q}$ and $\bar{q}_l = \frac{q_l}{q}$. For nontrivial solutions of Equation (3-5) the secular determinant must vanish :

$$\left|C_{iklm} \bar{q}_k \bar{q}_l - \rho v^2 \delta_{im}\right| = 0 \tag{3-6}$$

The above equation has three roots v_l corresponding to the sound velocities of the three acoustic modes. In terms of the 6-components notation for C_{iklm} , the determinant becomes;

$$\begin{vmatrix} \lambda_{11}-\rho v^2 & \lambda_{12} & \lambda_{13} \\ \lambda_{12} & \lambda_{22}-\rho v^2 & \lambda_{23} \\ \lambda_{13} & \lambda_{23} & \lambda_{33}-\rho v^2 \end{vmatrix} = 0 \qquad (3\text{-}7)$$

where λ_{ij} are given by[19],

$$\lambda_{11} = \bar{q}_x^2 C_{11} + \bar{q}_y^2 C_{66} + \bar{q}_z^2 C_{55} + 2\bar{q}_y\bar{q}_z C_{56} + 2\bar{q}_x\bar{q}_z C_{15} + 2\bar{q}_x\bar{q}_y C_{16} ;$$

$$\lambda_{22} = \bar{q}_x^2 C_{66} + \bar{q}_y^2 C_{22} + \bar{q}_z^2 C_{44} + 2\bar{q}_y\bar{q}_z C_{24} + 2\bar{q}_x\bar{q}_z C_{46} + 2\bar{q}_x\bar{q}_y C_{26} ;$$

$$\lambda_{33} = \bar{q}_x^2 C_{55} + \bar{q}_y^2 C_{44} + \bar{q}_z^2 C_{33} + 2\bar{q}_y\bar{q}_z C_{34} + 2\bar{q}_x\bar{q}_z C_{35} + 2\bar{q}_x\bar{q}_y C_{45} ;$$

$$\lambda_{12} = \bar{q}_x^2 C_{16} + \bar{q}_y^2 C_{26} + \bar{q}_z^2 C_{45} + \bar{q}_y\bar{q}_z(C_{46} + C_{25}) + \bar{q}_x\bar{q}_z(C_{14} + C_{56}) + \bar{q}_x\bar{q}_y(C_{12} + C_{66}) ;$$

$$\lambda_{13} = \bar{q}_x^2 C_{15} + \bar{q}_y^2 C_{46} + \bar{q}_z^2 C_{35} + \bar{q}_y\bar{q}_z(C_{45} + C_{36}) + \bar{q}_x\bar{q}_z(C_{13} + C_{55}) + \bar{q}_x\bar{q}_y(C_{15} + C_{56}) ;$$

$$\lambda_{23} = \bar{q}_x^2 C_{56} + \bar{q}_y^2 C_{24} + \bar{q}_z^2 C_{34} + \bar{q}_y\bar{q}_z(C_{44} + C_{23}) + \bar{q}_x\bar{q}_z(C_{36} + C_{45}) + \bar{q}_x\bar{q}_y(C_{25} + C_{46}) .$$

After solving Equation (3-7) for the eigenvalues ρv_i^2, these can then be substituted back into Equation (3-6) and one obtains the displacement eigenvectors $\vec{u}$.

In most experiments $\vec{q}$ is chosen along a high symmetry direction. $\vec{u}$ will either be parallel or perpendicular to $\vec{q}$. The first case corresponds to the longitudinal displacement of the atoms in the crystal while the second case corresponds to the two transverse acoustic modes. Later on we will see how we can select each one of these modes separately. At the moment let us use the symmetry of our crystal to simplify Equation (3-7). The

elastic constant tensor for the $\bar{4}2m$ point group is as follows[18],

$$(C_{ij}) = \begin{pmatrix} C_{11} & C_{12} & C_{13} & 0 & 0 & 0 \\ C_{12} & C_{11} & C_{13} & 0 & 0 & 0 \\ C_{13} & C_{13} & C_{33} & 0 & 0 & 0 \\ 0 & 0 & 0 & C_{44} & 0 & 0 \\ 0 & 0 & 0 & 0 & C_{44} & 0 \\ 0 & 0 & 0 & 0 & 0 & C_{66} \end{pmatrix} \tag{3-8}$$

The wavevector for our configuration (see Figure 4) is

$$\vec{q} = \frac{1}{\sqrt{2}}(1,1,0) \tag{3-9}$$

Using Equations (3-8) and (3-9) to solve Equation (3-7), we get the following three eigenvalues for the velocities of sound in the crystal.

$$\rho v_L^2 = \tfrac{1}{2}\left[C_{11} + C_{66} + (C_{12} + C_{66})\right] \tag{3-10a}$$

$$\rho v_{T1}^2 = \tfrac{1}{2}\left[C_{11} + C_{66} - (C_{12} + C_{66})\right] \tag{3-10b}$$

$$\rho v_{T2}^2 = C_{44} \tag{3-10c}$$

where the subscripts L and T stand for longitudinal and transverse, respectively. In the present study we are only interested in the longitudinal mode corresponding to Equation (3-10a). For simplicity we will drop the subscript on v and define

$$C \equiv \tfrac{1}{2}\left[C_{11} + C_{66} + (C_{12} + C_{66})\right] \tag{3-11}$$

so that Equation (3-10a) can be written more simply;

$$\rho v^2 = C \tag{3-12}$$

Frequency Shift and Wavevector

We have already shown how the elastic constants are

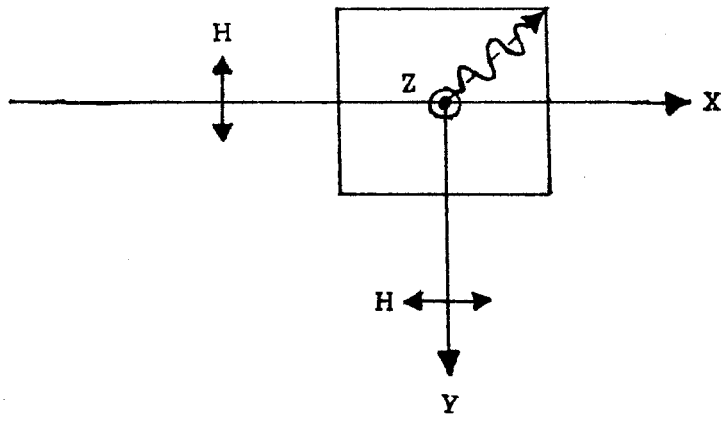

Figure 4. LA[110] Phonon Configuration for the Right Angle Scattering Geometry. Shown Is the Top View of the RADP Sample Along the z-Axis. The Incident and Scattered Light Are Both Horizontally Polarized (HH). The Wiggly Line Represents the Phonon Direction of Propagation

related to the velocities of sound. Now we need to show how the phonon frequency relates to both. In the long wavelength limit the following relation is satisfied[17],

$$\omega_q = qv$$

$$\text{or, } v = \frac{\omega_q}{q} \tag{3-13}$$

where v, ω_q and q are respectively the phonon velocity, frequency and wavevector. By measuring ω_q we can calculate v from Equation (3-13) knowing the magnitude of the wave vector. We will now proceed to show how this can be done.

A quantum mechanical description of Brillouin scattering is based on the following three consecutive processes: 1)Photon absorption, 2)Phonon absorption or emission and 3)Photon emission. A schematic of these processes is shown in Figure 5. From the energy and momentum considerations we have,

$$\omega_s = \omega_o \pm \omega_q \tag{3-14a}$$

$$\vec{k}_s = \vec{k}_o \pm \vec{q} \tag{3-14b}$$

where the (-) sign corresponds to the Stokes event and the (+) sign corresponds to the Antistokes event. Also from Figure 5 we can see that,

$$\left|\vec{q}\right| = \left|\vec{k}_o - \vec{k}_s\right| \cong 2\left|\vec{k}_o\right| \sin\frac{\theta}{2} \tag{3-15}$$

In terms of the wavelength of the incident light $\left|\vec{k}_o\right| = \frac{2\pi n}{\lambda_o}$; where n is the index of refraction of the

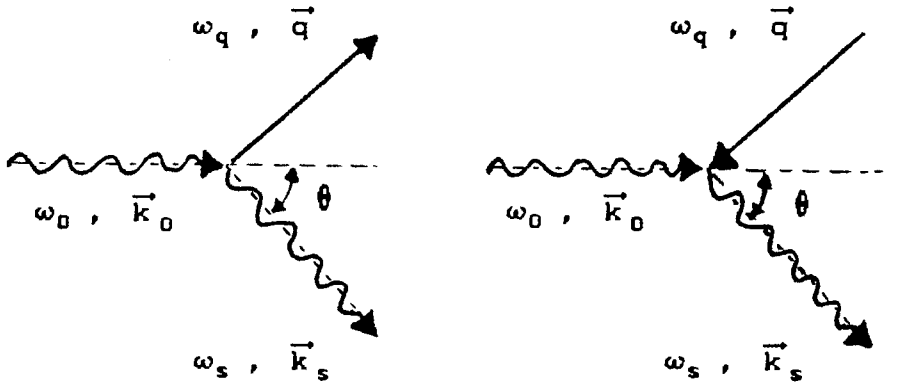

Figure 5. Diagrams of First-Order Photon Scattering by Phonons

material. Substituting this into Equation (3-15) we get;

$$\left|\vec{q}\right| = q \approx \frac{4\pi n}{\lambda_o} \sin\frac{\theta}{2} \qquad (3\text{-}16a)$$

From the above equation we can see that the phonon wavevector is restricted to the values between 0 (at $\theta=0$ for forward scattering) and $\frac{4\pi n}{\lambda_o}$ (at $\theta=\pi$ for backscattering). For the right angle configuration used in our experiments, $\theta=\frac{\pi}{2}$ and the wavevector becomes,

$$q = \frac{2\pi}{\lambda_o} \sqrt{2}\, n \qquad (3\text{-}16b)$$

It is important to note here that the phonon wavevector is completely determined if we know the index of refraction of the sample , the wavelength of the incident laser beam and the scattering angle θ. The direction of $\vec{q}$ is determined by the orientation of the crystal. Now we substitute Equation (3-16b) into Equation (3-13) and get;

$$v = \frac{\sqrt{2}\lambda_o}{4\pi n}\, \omega_q \qquad (3\text{-}17)$$

All we have to do now is measure ω_q from a Brillouin spectrum such as the one in Figure 6. The phonon frequency is then given by

$$\omega_q = \mathrm{FSR}\, \frac{\ell}{L} \qquad (3\text{-}18)$$

where ℓ is the LA phonon frequency (in channel numbers) measured relative to the central Rayleigh peak, L is the number of channels between two consecutive Rayleigh peaks and FSR is the free spectral range defined as,

$$\mathrm{FSR} = \frac{1}{2n_o d} = \frac{1}{2d} \qquad (3\text{-}19)$$

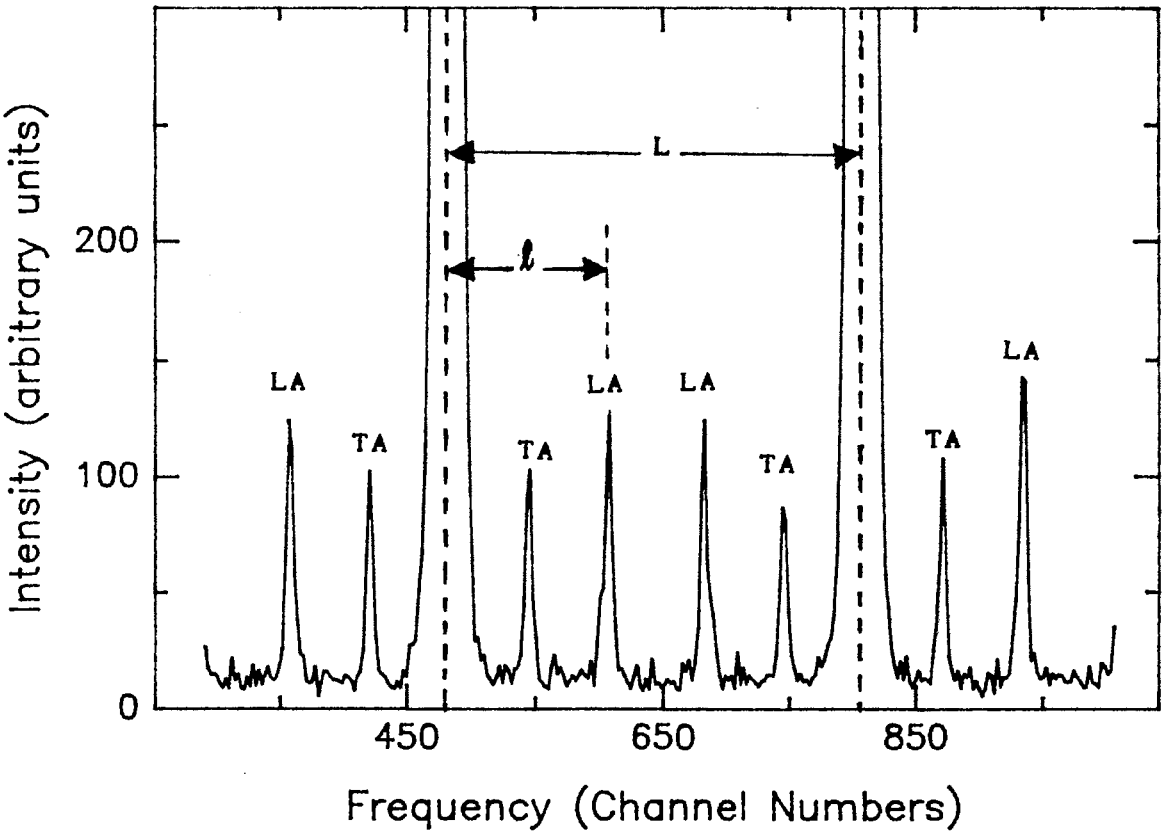

Figure 6. Typical Brillouin Spectrum from an RADP Sample (x=0.28). LA and TA Stand for Longitudinal and Transverse Acoustic Phonons Respectively. The Incident Light Was Horizontally Polarized

where d is the Fabry-Perot (FP) plate separation. In the last part of Equation (3-19) we used n_o=1 for air between the FP plates. Combining Equations (3-18) and (3-19) we have;

$$\omega_q = \frac{\ell}{2dL} \qquad (3\text{-}20)$$

By measuring ℓ and L directly from a Brillouin spectrum and knowing the plate separation one obtains the phonon frequency ω_q.

Rayleigh Ratio

The intensity of the components in the scattering spectrum is rather important. It allows us to set up the polarization selection rules. The quantity that provides this information is called the Rayleigh ratio, or the differential cross section per unit volume given by[19],

$$R_{\alpha\beta} = \left(\frac{1}{V}\right)\frac{d\sigma}{d\Omega} = r^2\,\frac{I_s^{\alpha}}{VI_o^{\beta}} \qquad (3\text{-}21)$$

where α and β are respectively the directions of polarization for the scattered (I_s) and incident (I_o) light. V is the scattering volume from which light is being collected and r is the distance from the scattering volume to the detector.

Considering the changes in the dielectric constant caused by the stress and strain due to the propagating modes in the crystal, and using the photoelastic coupling of these, one can express Equation (3-21) in the following

useful form[19,20]:

$$R^j = \frac{k_B T \omega_s^4}{32\pi^2 c^4 \rho v_j^2}\left[\hat{e}_s \cdot T^j \cdot \hat{e}_o\right]^2 \left(\frac{n_s}{n_o}\right) \qquad (3\text{-}22)$$

where the superscript j stands for the j^{th} acoustic mode (j=1,2 and 3) with velocity v_j. $\hat{e}_o$ and $\hat{e}_s$ are the unit vectors in the directions of the polarization of the incident and scattered light, k_B is Boltzman constant, T is the sample temperature, ω_s is the angular frequency of the scattered light in vacuum, ρ is the mass density of the crystal, n_o and n_s are the indices of refraction for the incident and scattered light respectively, and T is the scattering tensor which can be expressed[19] in terms of the reciprocal of distortions in the dielectric tensor of the crystal. For high symmetry directions the scattering tensor and the corresponding elastic constants are tabulated for each of the crystal classes by Cummins and Schoen[19].

In the $\bar{4}2m$ symmetry class, the xy-phonon, with $\vec{q}=(1,1,0)$ wave vector, has the following scattering T-tensor[19]:

$$T = \frac{1}{2}\begin{pmatrix} \epsilon_o^2(p_{11}+p_{12}) & 2\epsilon_o^2 p_{66} & 0 \\ 2\epsilon_o^2 p_{66} & \epsilon_o^2(p_{11}+p_{12}) & 0 \\ 0 & 0 & 2\epsilon_e^2 p_{31} \end{pmatrix} \qquad (3\text{-}23)$$

where p_{ij} are the photoelastic constants. In the configuration of our experiment, shown in Figure 4, $\hat{e}_s=(1,0,0)$ and $\hat{e}_o=(0,1,0)$. Substituting these along with Equation (3-23) into Equation (3-22) we have,

$$R \propto \left[\hat{e}_s \cdot T \cdot \hat{e}_o\right]^2 = \left[2\epsilon_o^2 p_{66}\right]^2$$

This means that the scattering intensity of this component is non-zero and it is an allowed mode. We can also show that in this case the two transverse modes are polarization forbidden.

Brillouin Scattering in KDP-Type Ferroelectrics

In the case of a ferroelectric crystal, some of the equations listed earlier have to be modified. KDP-type crystals are piezoelectric at all temperatures. This makes it necessary to include both their elastic and dielectric response together. The constitutive equations up to 2nd order in polarization are[7];

$$\chi^{-1}_{ij}P_j - h_{ikl}e_{kl} - 2R_{ijkl}P_je_{kl} = E_i \qquad (3\text{-}24a)$$

$$-h_{ikl}P_i - R_{ijkl}P_iP_j + C_{klmn}e_{mn} = \sigma_{kl} \qquad (3\text{-}24b)$$

where the strain e and the polarization P are the independent variables. χ is the dielectric susceptibility tensor of the unpolarized crystal. C, σ, h and R tensors are respectively the elastic, stress, piezoelectric and electrostriction constants. The temperature dependence is taken into account through these coupling coefficients. For the elastic constants this temperature dependence is mainly due to lattice anharmonicity. The crystal symmetry $\bar{4}2m$, allows two non-zero components of the dielectric susceptibility namely; $\chi_{11}=\chi_1$ and $\chi_{33}=\chi_3$. The piezoelectric

tensor has the following form[1];

$$\begin{pmatrix} 0 & 0 & 0 & h_{14} & 0 & 0 \\ 0 & 0 & 0 & 0 & h_{14} & 0 \\ 0 & 0 & 0 & 0 & 0 & h_{36} \end{pmatrix}$$

so that there are only two non-zero components; $h_{14}=h_{25}$ and h_{36}, and R has[1] 7 distinct non-zero components while C has 6 as shown in Equation (3-8).

At first we will look at the changes in the equations of motion for R=0 and derive some of the equations that would be needed for the data analysis. Then at the end of this section we will carry out a formal discussion of the contributions of R.

From this point on we will be using the 6-component tensor notation (see for example Reference 18 or 20). In our experimental configuration we need only consider σ_6 component of stress and the corresponding field component E_3. Since ω, the measuring frequency, is small compared to the resonant frequencies of the sample, there cannot be any stress on the sample. Setting R=0 and $\sigma_6=0$ in Equation (3-18) we get,

$$\chi^{-1}P_3 - h_{36}e_6 = E_3 \qquad (3\text{-}25a)$$

$$-h_{36}P_3 + C_{66}e_6 = 0 \qquad (3\text{-}25b)$$

where we have considered only non-zero diagonal elements.

From dielectric measurements[21], it has been shown that the distribution of relaxations have caused dispersion and loss in the low-frequency dielectric constant observed below 30 K. As the temperature is increased the relaxation

times become shorter and shorter up to a certain temperature ($T \sim 100K$) above which the system becomes fully relaxed and χ can be taken independent of ω.

As it is generally done[22,23] in the case of KDP, we similarly define a dimensionless inverse coupling constant Q by,

$$Q \equiv \frac{C}{\chi(0,T)h_{36}^2} \tag{3-26}$$

where C is given in Equation (3-11). We also define a 'free' dielectric susceptibility by,

$$\chi_{FR}^{-1}(\omega,T) \equiv \frac{E_3}{P_3} \tag{3-27}$$

Using Equations (3-25a), (3-26) and (3-27), we can relate the 'free' and coupled susceptibilities through the coefficient Q as follows,

$$\chi_{FR}(0,T) = \frac{Q}{Q-1}\chi(0,T) \tag{3-28}$$

We can see clearly from Equation (3-28) that χ_{FR} diverges at Q=1 corresponding to the ferroelectric phase while Q>1 corresponds to the paraelectric phase.

The equations of motion for a piezoelectric material are[7]:

$$\chi^{-1}(\omega,T)\delta P - h\delta e = \delta E \tag{3-29a}$$

$$-h\delta P + \left(C - \frac{\rho\omega^2}{q^2}\right)\delta e = \delta\sigma \tag{3-29b}$$

where δP and δe are incremental changes in the fields, δE and $\delta\sigma$ are the corresponding changes in the forces and ρ is the mass density of the crystal.

The phonon frequency in a non-piezoelectric material is

a very useful quantity defined as,

$$\omega_a = q\sqrt{\frac{C}{\rho}} \tag{3-30}$$

This is called the bare or uncoupled phonon frequency. Its temperature dependence can be described by a Debye anharmonic approximation[7] as follows;

$$\omega_a(T,x) = \omega_a(0,x)\left[1 - A\theta(x)F\left(\frac{\theta(x)}{T}\right)\right] \tag{3-31}$$

where θ is the Debye temperature and F is the Debye integral given by

$$F(x) = \frac{3}{x^4}\int_0^x \frac{u^3}{e^u - 1}\,du \tag{3-32}$$

In Chapter V, we will find Equation (3-31) very useful in fitting our high temperature data.

The line shape of the scattered spectrum as given by E.Courtens et al.[7] is the following,

$$I(\omega,T) \propto \frac{k_B T}{\pi\omega}\frac{\kappa_I p^2}{\chi_0 h^2}\frac{\left[1 + \gamma\left(1 - \frac{\omega^2}{\omega_a^2}\right)\right]^2}{\left[\kappa_R + \frac{\chi_B}{\chi_0} - Q\left(1 + \frac{\chi_B}{\chi_0}\right)\left(1 - \frac{\omega^2}{\omega_a^2}\right)\right]^2 + \kappa_I^2} \tag{3-33}$$

where p is just the photoelastic constant p_{66} and a is the electro-optic constant a_{36}. γ determines the relative strength of the coupling constants,

$$\gamma = \frac{aC}{ph} \tag{3-34}$$

κ on the other hand is a relaxation function defined by[7,25];

$$\kappa = \kappa_R + i\kappa_I = \int_0^{\infty} \frac{g(\tau, T)}{1 - i\omega\tau} \, d\ln\tau \qquad (3\text{-}35)$$

where $g(\tau,T)$ is a broad distribution of Debye relaxations of characteristic time τ normalized to 1 upon integration over $d\ln\tau$.

The spectrum shape is primarily affected by the zeros of the denominator in Equation (3-33). In other words the Brillouin peak is located at $\omega=\omega_B$ such that

$$\kappa_R + \frac{\chi_B}{\chi_0} - Q\left(1 + \frac{\chi_B}{\chi_0}\right)\left(1 - \frac{\omega^2}{\omega_a^2}\right) = 0 \qquad (3\text{-}36)$$

As it was mentioned earlier: at high temperatures ($T>100K$), the relaxation times become very small and Equation (3-35) can be approximated by $\kappa\sim 1$. Substituting this result into Equation (3-36) and solving for ω_B we have

$$\omega_B \cong \omega_a\sqrt{\frac{Q-1}{Q}} \qquad (3\text{-}37)$$

This is a very important equation that relates the coupled (measured) phonon frequencies to the uncoupled (bare) phonon frequencies through the inverse coupling constant Q which can be obtained from dielectric measurements[8].

In the previous discussion we assumed R=0 so that only the piezoelectric coupling was considered. Now we like to include electrostriction ($R\neq 0$) and discuss its contributions to the Brillouin spectra. In this case the equations of motion (Equations (3-29)) become nonlinear and cannot be solved exactly. Meanwhile an estimate of the elastic stiffness changes (ΔC) can be obtained using Kubo's formalism[24].

Due to the glassy nature of RADP below T_D=100 K, the polarization fluctuation δP can be written as follows,

$$\delta P(t) = \delta P^s + \delta P^d(t) \qquad (3\text{-}38)$$

where δP^s are static polarization fluctuations that depend on the space coordinates only.

In view of Equation (3-38) and References 24 and 25 two contributions to the elastic stiffness were obtained,

$$\Delta C = \Delta C^d + \Delta C^{LK} \qquad (3\text{-}39)$$

where ΔC^d is strictly dynamic arising from δP^d and ΔC^{LK} is a Landau-Khalatnikov (LK) term[26] which below a phase transition involves an Edwards-Anderson (EA) order parameter[9] defined as follows,

$$q_m^{EA} = V^{-1} \int \left[\delta P_m^s(\vec{r}) \right]^2 d^3r \qquad (3\text{-}40)$$

where the integral is over the volume V.

From a fitting to the Brillouin frequency data for the LA[100] phonon, It was shown[25] that the LK term in Equation (3-39) was the dominant one and that ΔC^d was not needed and could be neglected. The elastic stiffness change due to electrostriction is then given by the following[25] for $q \to 0$,

$$\Delta C^{LK}_{ijkl}(0,\omega) \cong -4R_{ijmn}R_{klmn}\kappa_1(\omega)q_m^{EA}\chi_{nn}(0) \qquad (3\text{-}41)$$

Similarly, the elastic stiffness changes associated with the piezoelectric coupling is written as follows[24],

$$\Delta C^{P}_{ijkl} \cong -h_{nij}h_{nkl}\chi_{nn}(0) \qquad (3\text{-}42)$$

In the case of our study, as we showed earlier, the only relevant nonzero piezoelectric constant is $h_{36}=h$ so that Equation (3-42) becomes simply,

$$\Delta C^{P}_{66} \cong -h^2\chi_3 \qquad (3\text{-}43)$$

where, we set $\chi_{nn}=\chi_n$ and performed the summation over the indices.

Comparing Equations (3-41) and (3-42), we see that the LK term has just a form of an additional piezoelectric contribution. This can be taken into account by an additional term added to the piezoelectric constant. Dropping all indices for simplicity we have for the elastic stiffness changes,

$$\Delta C \cong \Delta C^{P} + \Delta C^{LK} \qquad (3\text{-}44)$$

by setting $\Delta C=-h^2_{eff}\chi_3$ we get,

$$h^2_{eff} = h^2 + 4R^2\kappa_1 q^{EA} \qquad (3\text{-}45)$$

The electrostriction tensor for the tetragonal $\bar{4}2m$ crytallographic class has the following form[18],

$$(R_{ij}) = \begin{pmatrix} R_{11} & R_{12} & R_{13} & 0 & 0 & 0 \\ R_{12} & R_{11} & R_{13} & 0 & 0 & 0 \\ R_{31} & R_{31} & R_{33} & 0 & 0 & 0 \\ 0 & 0 & 0 & R_{44} & 0 & 0 \\ 0 & 0 & 0 & 0 & R_{44} & 0 \\ 0 & 0 & 0 & 0 & 0 & R_{66} \end{pmatrix} \qquad (3\text{-}46)$$

Using Equation (3-46) along with the appropriate elastic constant C given in Equation (3-11) we can express the correction to the piezoelectric constant shown in

Equation (3-45) more precisely by the following,

$$R^2 q^{EA} = \left(\frac{1}{2}(R_{11} + R_{12})^2 + 2R_{66}^2\right) q_1^{EA} \frac{x_1}{x_3} + R_{31}^2 q_3^{EA} \qquad (3\text{-}47)$$

It was shown in Reference 6 that the TA[100] phonon was controlled by C_{66} elastic constant. Thus, this phonon coupling to the polarization was almost entirely of piezoelectric nature suggesting that the corresponding electrostriction term R_{66} is very small. On the other hand it was shown in Reference 25 that the LA[100] phonon was controlled by C_{11} and, therefore, was coupled to the polarization mainly through electrostriction.

The above discussion suggests that the LA[110] phonon which is controlled by a linear combination of C_{11}, C_{12} and C_{66} (see Equation (3-11)), is coupled to the polarization through both the piezoelectric and the electrostrictive effect. This is exactly what we have seen experimentally and will be discussed further in chapter V.

CHAPTER IV

DESCRIPTION OF EXPERIMENTS

Brillouin Scattering Setup

The light scattering setup used in these Brillouin experiments is shown schematically in Figure 7. A Spectra Physics model 2020 Argon-Ion laser was used to produce a single mode 5145Å line at a power of about 250 mW. Directly attached to the laser output was a Newport Broadband Polarization Rotator model PR-550, permitting adjustment of the laser output polarization with respect to the crystal optical axis. A 20cm focal length lens was used to focus the beam onto the sample mounted inside a custom made Janis He-Dewar model 8DT. A special sample mount was designed (see Appendix A for details) to prevent cracking of the sample due to large temperature changes. A Lake Shore temperature controller model DRC-91C was used to stabilize the temperature to ±0.01°K for several hours. A calibrated silicon diode sensor was mounted right behind the sample on a copper disk of about 0.2mm thickness (see Appendix A for details on the temperature control setup). Good thermal contact with the sample was achieved through a layer of a thermal compound made with a mixture of Crycon Copper Oxide

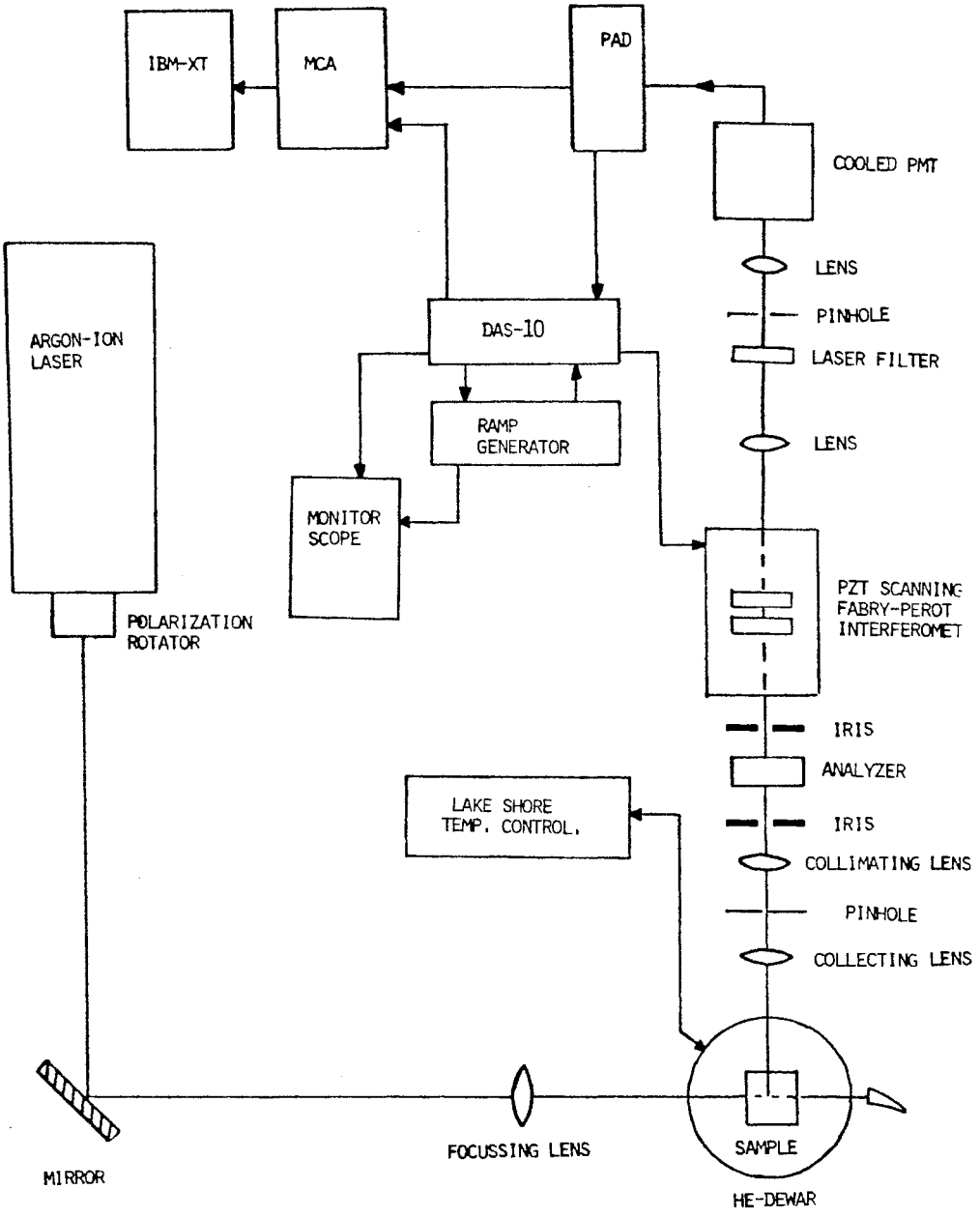

Figure 7. Experimental Apparatus for Right Angle Brillouin Scattering

and Apiezon N-grease. All temperatures quoted in this writing are accurate to better than ±0.5°K restricted mainly by the time allowed for stabilization.

A right angle scattering geometry was used. The scattered light was collected with an Olympus camera lens (f=5.5cm) through an iris which restricted the collected light to the size of the Fabry-Perot entrance which is 1.1cm. The lens then focuses the beam onto a 100 micron pinhole followed by another Olympus camera lens (f=5.0cm) used to collimate the collected light. A second iris was used to reduce the diameter of the collimated light even further (about 0.6cm) to help minimize the solid angle corrections[27] involved in the 90° scattering geometry (these corrections are important only in the sound velocity calculations).

After passing a polarization analyzer, the scattered light was frequency analyzed in a piezoelectrically scanned Burleigh plane-parallel Fabry-Perot (FP) interferometer operating in a triple pass mode. The scanning of the FP was accomplished with a Burleigh Programmable Ramp generator model RC-43 which applies a linear voltage to the three PZT stacks mounted behind the scanning mirror. Both 2-inch mirrors are broadband (450-550nm) coated for 93% reflection centered around the 5145Å and reaching about 95% at this wavelength. The plate spacing used in most experiments was 0.368 cm corresponding to a free spectral range of 1.359 cm^{-1} or 41 GHz. The output of the FP was then focused

onto a 500 micron pinhole. A 1nm bandwidth laser filter centered on the 5145Å wavelength, was placed right before the pinhole to block out high-frequency Raman-scattered lines. An iris-lens assembly was attached to the Photomultiplier (PMT) housing. The iris' function was to seal off the PMT and protect it from room light when not in use. The lens however was used to focus the transmitted light from the pinhole onto the surface of the S-20 photocathode of an ITT FW-130 PMT tube. A voltage of -1950 volts was always applied to the PMT. The latter was also water cooled to -24°C by a Products For Research cooling unit model TE104RF, keeping the dark count at about 1.5 counts/sec. The output of the PMT is then connected to the photon-counting electronics consisting of a Canberra Preamplifier-Amplifier-Discriminator (PAD) model 814 whose output was connected to both a ratemeter and a Burleigh DAS-10 stabilization system for the FP. The discriminator output on the other hand, was connected to a Canberra Multichannel-Analyser (MCA) model 3502 for data acquisition. An IBM-XT was then interfaced to the MCA for data storage and analysis.

The crystal orientation used in these experiments is shown in Figure 4. This x(y,x)y geometry allows us to look exclusively at the longitudinal wave propagating along the $(\hat{x}-\hat{y})/\sqrt{2}$ direction (called the xy acoustic phonon). This configuration is similar to the one commonly used in Raman scattering experiments to observe the B_2 soft mode in KDP[28].

Index of Refraction Measurements

The room temperature indices of refraction were measured using a slight variation of the minimum angle of deviation technique used for a prism shaped sample. The advantage of this variation is that it uses a 90° edge of the sample instead of a 60° angular cut. The method[29] consists of two high quality equilateral fused quartz prisms placed against each other so that they form a right angle with one of their surfaces as shown in Figure 8b. The sample is placed so that two of its orthogonal faces ((100) and (010) faces) lean against the two prisms' surfaces which are making a right angle. The samples optic axis is along the [001] direction. A partial index matching oil was used to enhance the surface to surface contact and avoid multiple reflections at the interfaces. Both prisms have the same index of refraction (n_1=1.5202).

The whole sample assembly was placed on an adjustable optical stage of a conventional spectroscope made by Gaertner-Peck series 87015-02. A portion of the beam, coming from the same Argon-Ion laser described earlier operating at the same wavelength, was redirected across to another table for this type of measurement. The beam was first collimated then attenuated by neutral density filters (ND). The parallel beam of light then enters a vertical slit followed by a collimator attached to the spectroscope, then passes through the sample assembly described above. The schematics

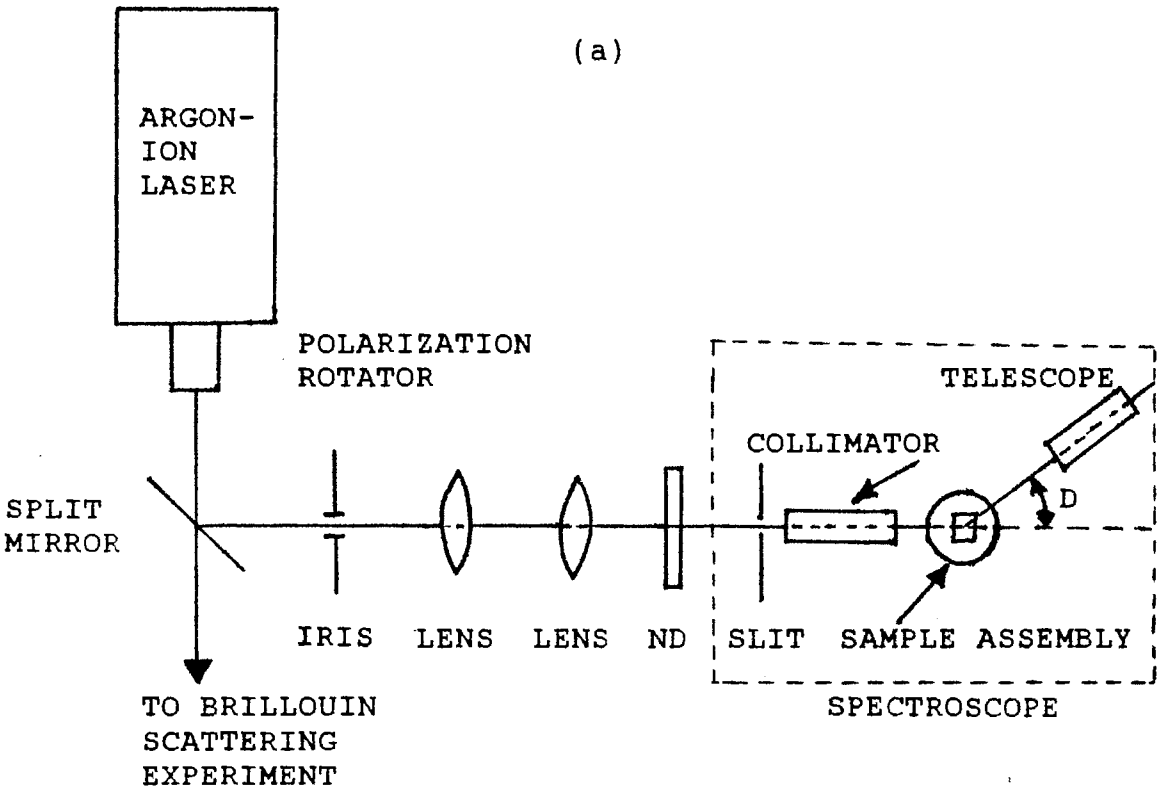

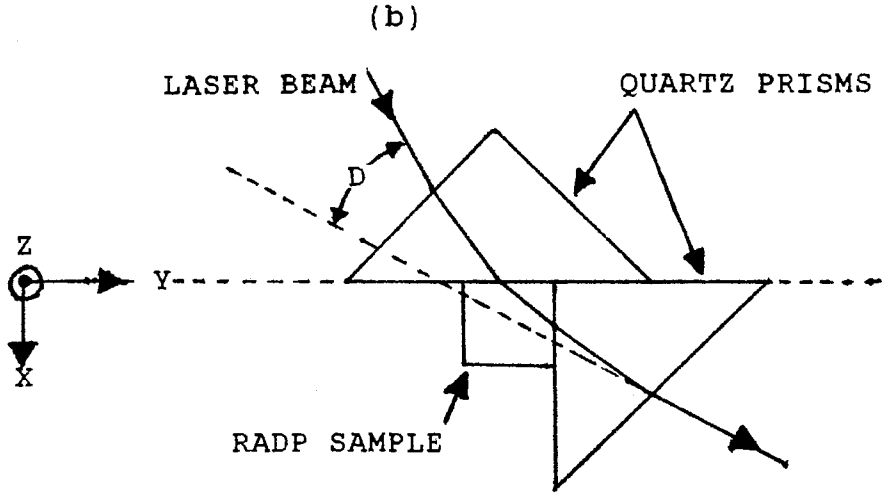

Figure 8. (a) Experimental Apparatus for the Index of Refraction Measurements and (b) an Enlargement of the Sample Assembly Cross Section

of this is shown in Figure 8a. The minimum angle of deviation D was then measured and the sample index of refraction was computed from the following equation[29]:

$$n = \sin(D/2) + \left(n_1^2 - \sin^2(D/2)\right)^{1/2} \qquad (4\text{-}1)$$

The incident beam with polarization parallel to the c-axis (i.e. optic axis) of the crystal allowed us to measure the extraordinary index of refraction (n_e). On the other hand, we were unable to measure the ordinary index of refraction (n_o) by this method due to the very small deviation angle. Alternatively, we calculated these indices using the Brillouin scattering data. Let $\Delta\omega_o$ and $\Delta\omega_e$ respectively be the Brillouin frequency shift for the Horizontal-Horizontal (HH) and Vertical-Vertical (VV) incident-scattered light polarizations. Then from Equation (3-17) we have,

$$\rho v^2 = \frac{\rho c^2 \lambda_o^2}{2n_o^2} (\Delta\omega_o)^2 \qquad (4\text{-}2)$$

$$\rho v^2 = \frac{\rho c^2 \lambda_o^2}{2n_e^2} (\Delta\omega_e)^2 \qquad (4\text{-}3)$$

Equating the right hand sides of the above equations and simplifying we get

$$\frac{(\Delta\omega_o)^2}{n_o^2} = \frac{(\Delta\omega_e)^2}{n_e^2}$$

$$\text{or, } n_o = \frac{\Delta\omega_o}{\Delta\omega_e} n_e \qquad (4\text{-}4)$$

The results of these calculations are shown in Table I.

TABLE I

PHYSICAL CONSTANTS OF RADP SAMPLES

Concentration (% Weight)	Density (g/cm^3)	Indices of Refraction* Ordinary (n_o)	Extraordinary (n_e)
0.00	2.869	1.510	1.4815
0.28	2.451	1.517	1.4822
0.42	2.288	1.529	1.4822
0.48	2.217	1.508	1.4819
1.00	1.786	1.527	1.4820

*For the wavelengh λ=5145Å

Density Measurements

These simple but important experiments allowed us to determine the different concentrations of our samples. The method[30] consists of determining the density of our crystals by means of the Buoyancy technique. This uses Archimedes' principle that a solid immersed in a fluid experiences an upwards force equal in magnitude to the weight of the displaced fluid ΔW. The apparent loss in weight of the solid is then due to this upwards force. If ρ_F and ρ_S are respectively the densities of the fluid and the solid then :

$$\rho_S(W_a - W_F) = W_a\rho_F \qquad (4\text{-}5)$$

where W_a and W_F are respectively the weight of the solid in air and in the fluid. The volume of the displaced fluid is then $(W_a-W_F)/(g\rho_F)$ and that of the solid is just $W_a/(g\rho_S)$. Equating the two volumes we can solve for the density of the solid :

$$\rho_S = \frac{W_a}{W_a - W_F}\,\rho_F \qquad (4\text{-}6)$$

The solubility of our samples in water made it difficult to find a simple fluid for our measurements. The very low water content and a slow evaporation rate are the main requirements. Our best choice was a spectroscopic grade Cyclohexane with a density ρ_F=0.7726 gm/cm^3. From Equation (4-6) we can see that measuring the weights of our samples, inside and outside the fluid, is all we need to do in order

to determine their densities.

The weight measurements were carried out using a Mettler series AC100 Electronic Analytical balance with a standard deviation of ±0.1 mg. The mass of each sample was measured first in air then again inside the fluid. While lowering the samples into the fluid care had to be taken in order to avoid trapping air bubbles on their surfaces. Next we measured the weight of the wire itself (the one that was holding the sample) submerged to the same level of the fluid as before. This mass was then subtracted from our previous one for the sample plus wire to deduce the net sample weight inside the fluid.

Let us define ρ_1, ρ_2 and ρ respectively as the measured densities of ADP, RDP and RADP. These were then inserted into the following equation (see Appendix B for derivation)

$$\frac{m_1}{m_2} = -\left(\frac{1-\frac{\rho}{\rho_2}}{1-\frac{\rho}{\rho_1}} \right) \tag{4-7}$$

where m_1 and m_2 are, respectively, the masses of pure ADP and RDP content in the mixed crystals. The percent weight concentrations (x) are then expressed in terms of Equation (4-7) by the simple expression:

$$x = \frac{m_1}{m_1 + m_2} = \frac{\left(\frac{m_1}{m_2}\right)}{\left(\frac{m_1}{m_2}\right) + 1} \tag{4-8}$$

The results are listed in Table I.

CHAPTER V

RESULTS AND DISCUSSION

Frequency Versus Concentration

The room temperature Brillouin spectra for the concentrations x=0.28 and x=0.42 are shown respectively in Figures 9a and 9b. These spectra were obtained from the right angle scattering configuration described earlier. The Brillouin frequencies were measured with respect to the strong Rayleigh peak in the center. These frequencies are listed at two incident-scattered polarizations, (HH) and (VV), in Table II for x=0, 0.28, 0.42, 0.48 and 1. Plots of these data are shown in Figures 10a and 10b. The straight line represents a linear regression fit to the experimental data. The results of this linear fit were remarkable as one might notice.

The elastic constant C is expressed in terms of the Brillouin shift using Equations (3-12) and (3-17) as follows,

$$C = \rho v^2 = \frac{\lambda_0}{8\pi^2}\left(\frac{\omega_i}{n_i}\right)^2 \rho \qquad (5\text{-}1)$$

where i stands for 'ordinary' or 'extraordinary' for the index of refraction and the corresponding Brillouin frequency. The values of C listed in Table III were obtained

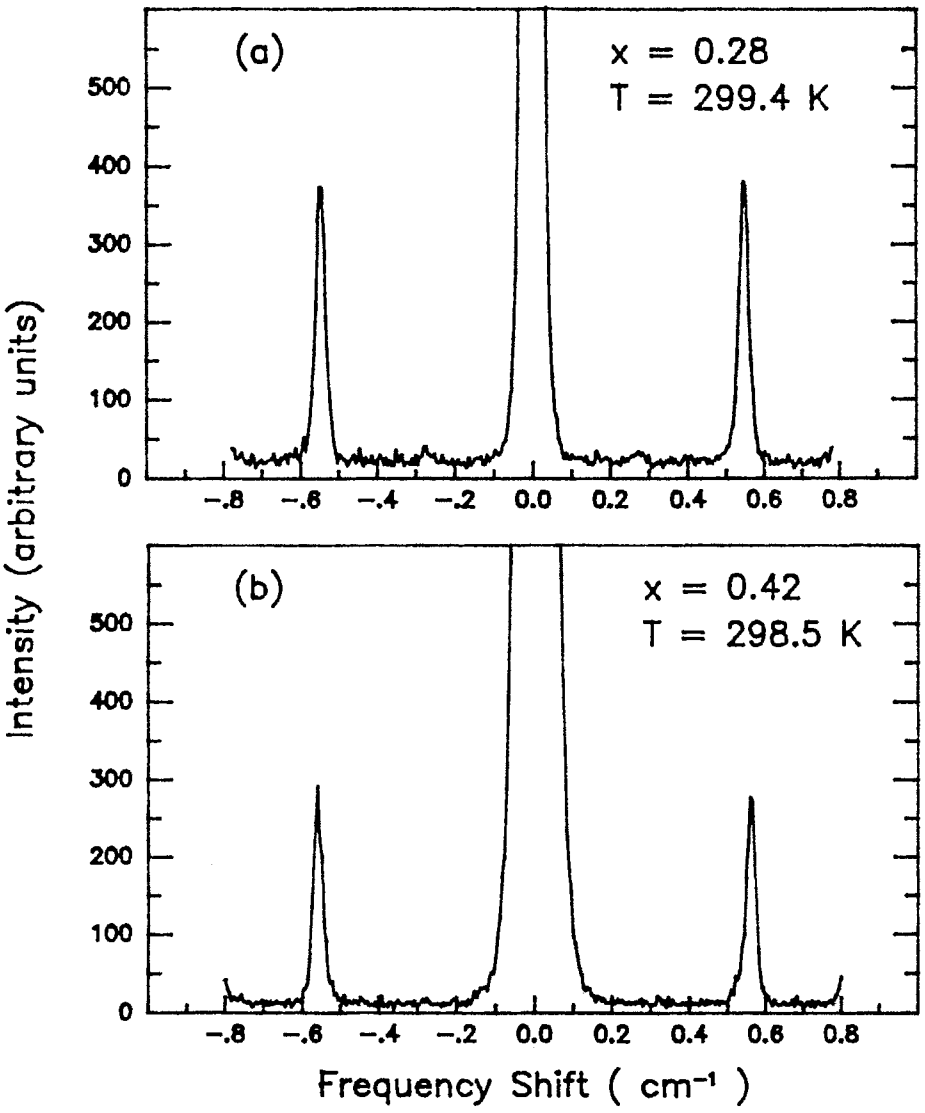

Figure 9. LA[110] Phonon Spectra of RADP for (a) x=0.28 and (b) x=0.42. The Incident and Scattered Light Polarizations are Both Horizontal

TABLE II

BRILLOUIN SHIFT FOR TWO INCIDENT-SCATTERED POLARIZATIONS: HORIZONTAL-HORIZONTAL (HH) AND VERTICAL-VERTICAL (VV)

Concentration (x) (% Weight)	ω_B (HH) (cm^{-1})	ω_B (VV) (cm^{-1})
0.00	0.479 ± 0.003	0.473 ± 0.003
0.28	0.543 ± 0.003	0.527 ± 0.003
0.42	0.574 ± 0.003	0.550 ± 0.003
0.48	0.572 ± 0.003	0.561 ± 0.003
1.00	0.674 ± 0.004	0.653 ± 0.004

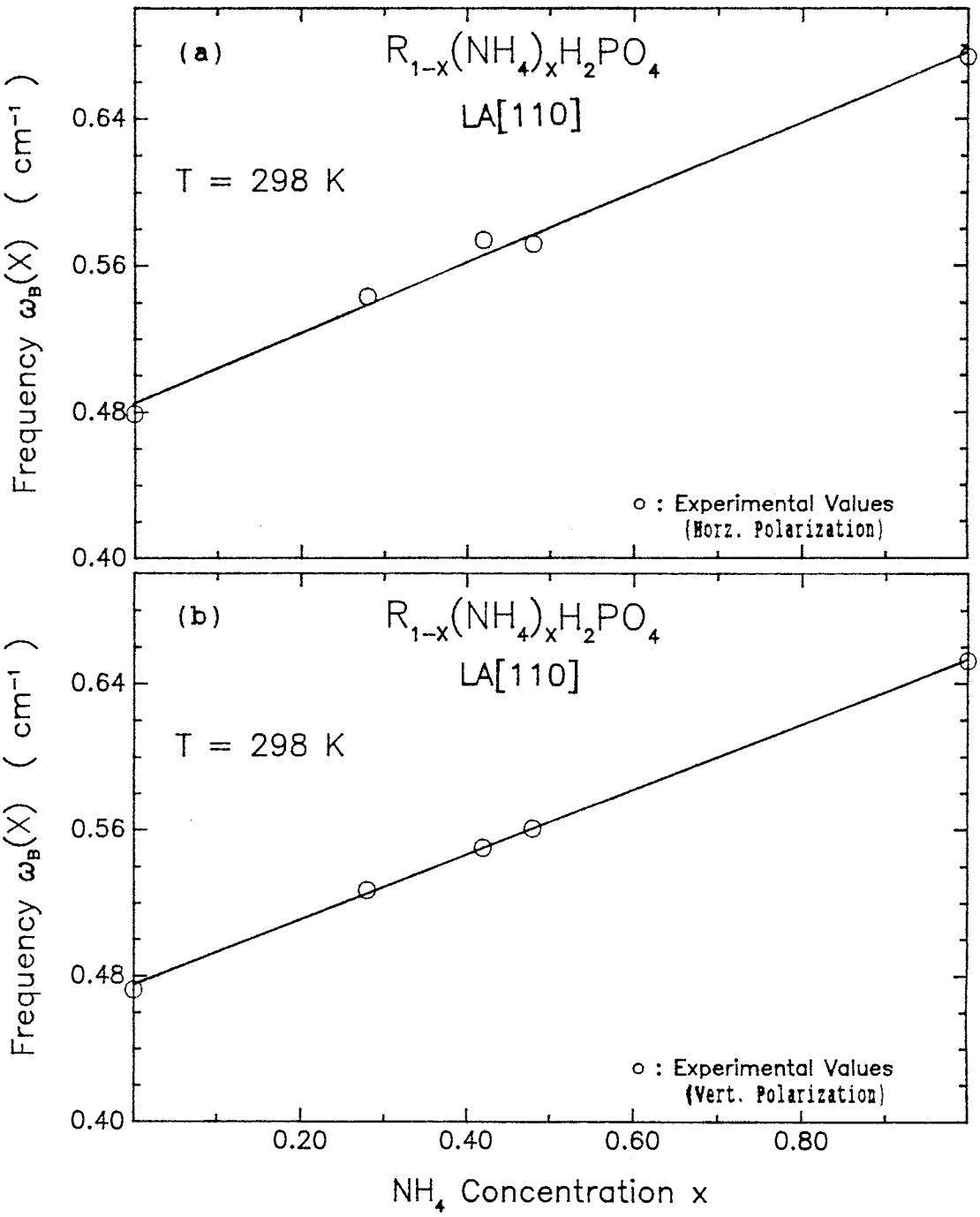

Figure 10. Frequency Shift (ω_B) Versus Ammonium Concentration (x) for Two Incident and Scattered Polarizations;
(a) Horizontal-Horizontal and
(b) Vertical-Vertical

TABLE III

EFFECTIVE ELASTIC CONSTANTS OF RADP CRYSTALS WITH DIFFERENT AMMONIUM CONCENTRATIONS (X)

Concentration (x) (% Weight)	$\frac{1}{2}[C_{11} + C_{12}] + C_{66}$ (10^{11} dyn/cm^2)
0.00	3.47 ± 0.05
0.28	3.69 ± 0.05
0.42	3.75 ± 0.05
0.48	3.78 ± 0.05
1.00	4.12 ± 0.06

from Equation (5-1) and a plot of these is shown in Figure 11. Again a linear regression fit was performed and a straight line resulted.

Next we can use Equations (4-7) and (4-8) to express ρ in terms of x. And we get,

$$\rho(x) = \frac{\rho_1\rho_2}{(\rho_2 - \rho_1)x + \rho_1} \qquad (5\text{-}2)$$

where ρ_1 and ρ_2 are respectively the densities of pure ADP and RDP. We note here that ρ_2 is larger than ρ_1 as can be seen in Table I.

Finally, by substituting Equation (5-2) into Equation (5-1) we can express C in terms of the NH_4 concentration x and the square of the ratio of the Brillouin frequency to the index of refraction as follows,

$$C(x) = \frac{\lambda_0}{8\pi^2}\left(\frac{\omega_i(x)}{n_i}\right)^2 \frac{\rho_1\rho_2}{(\rho_2 - \rho_1)x + \rho_1} \qquad (5\text{-}3)$$

From the values listed in Table I we can see that the x dependence of the index of refraction is very small and can be neglected. Equation (5-3) then suggests that C(x) must be linear if $\omega_i(x)$ is linear (see Figure 11). The origin of the linear behavior of C(x) is not as yet, known.

As we mentioned in Appendix B the unit cell volume changes very little going from RDP to ADP (i.e. $\frac{\Delta V}{V} \approx 0.006$) and can be considered constant. On the other hand, the atomic mass of Rb^+ (μ_1=85.039 amu) is much larger than that of NH_4^+ (μ_2=18.039 amu). The unit cell atomic mass decreases then by the amount $\delta\mu=\mu_1-\mu_2$ every time a Rb^+

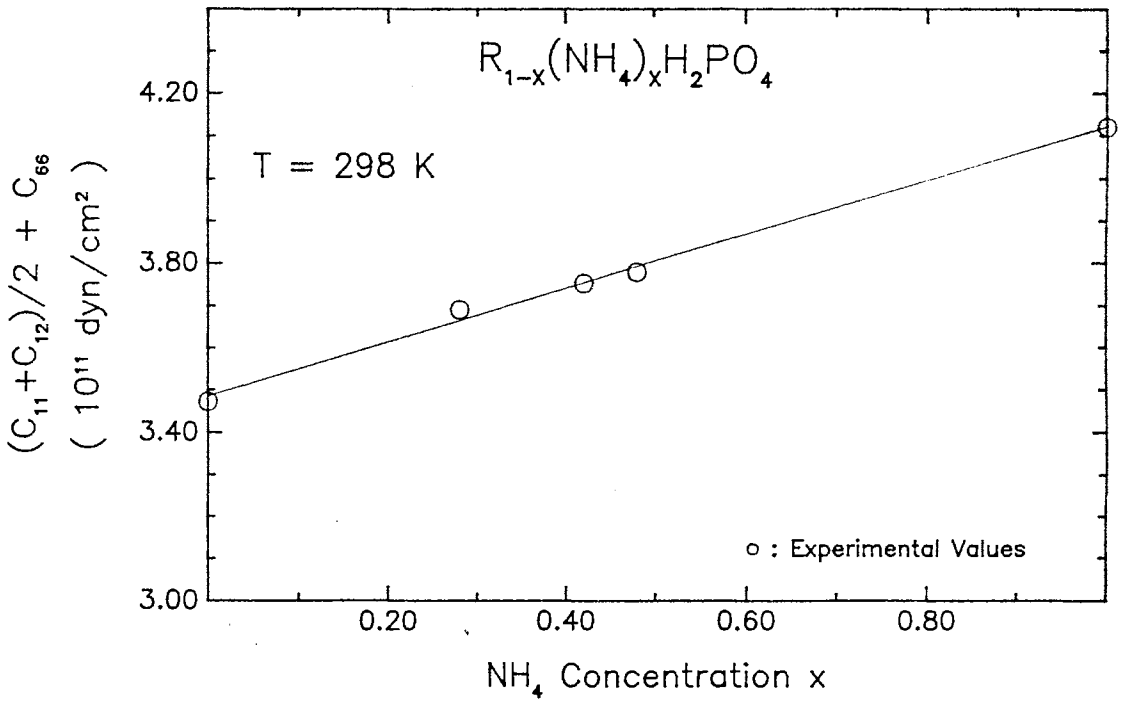

Figure 11. The Effective Elastic Constant Versus Ammonium Concentration (x)

ion is replaced by an NH_4^+ ion.

Frequency Versus Temperature

The temperature dependent experiments were also performed using the set up described in Chapter IV, starting from room temperature down to liquid-He temperatures. On cooling, the temperature was stabilized approximately every 5 degrees and a Brillouin spectrum was taken. The data was then analyzed using a fitting program to extract the Brillouin frequency shift. This fitting program is an extended and modified version of the one listed in Reference 27. The accumulated data for the two concentrations x=0.28 and x=0.42 are plotted in Figures 12a and 12b. The open circles represent the data taken using liquid-He as a cryogenic and the inverted triangle represents the data taken using liquid-N_2. The reason for using Liquid-N_2 is that it is easier to handle and costs much less than liquid-He. However, switching from one cryogenic to another requires a lot of care and several days of preparation. This means that the alignment of the experimental setup has to be done again every time the cryogenic was changed. It is important to note here that the data taken with the two different cryogenics matches very well at the common temperatures as seen in Figures 12a and 12b. These figures also show that some phonon softening occurs starting at about 150 K and reaches its maximum around 50 K for both concentrations. But below 50 K the phonon mode starts to

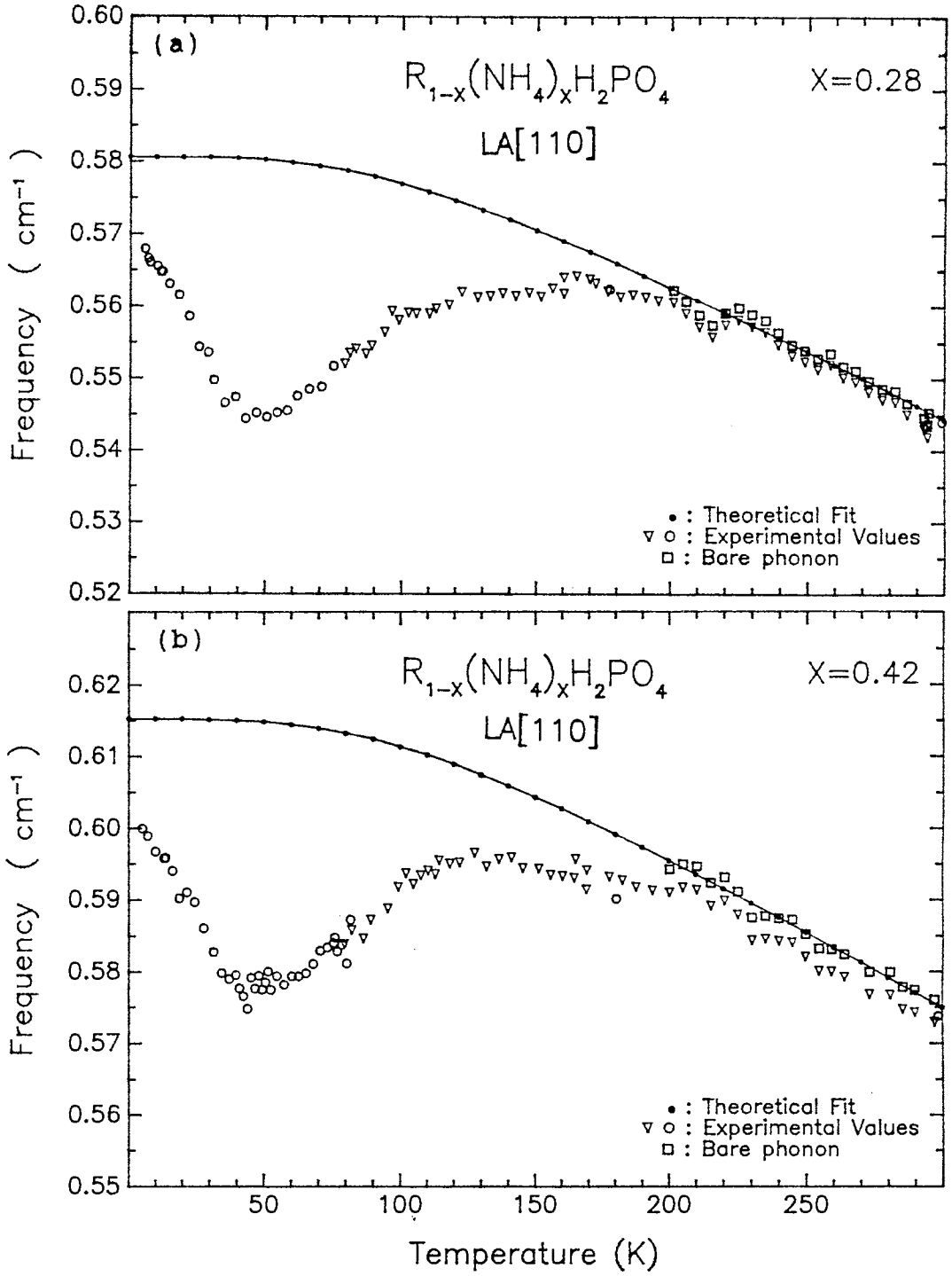

Figure 12. Frequency Shift Versus Temperature for (a) x=0.28 and (b) x=0.42. The Circles and Triangles Are the Measured Frequencies (ω_B) While the Squares Are the Calculated Bare Phonon Frequencies (ω_a). The Solid Line Is the Theoretical Debye Curve Explained in the Text

harden again until it reaches some limiting value at T=0 K.

Actual spectra of the antistokes Brillouin component are shown in Figures 13a and 13b for x=0.28 and x=0.42 respectively. The data shown here is for several temperatures between 81 K and 5K. Comparing the results for the two concentrations, we notice a relatively high background in the case of x=0.28. This is due to large polarization fluctuations which can be associated with the high Rb^+ ion concentration as in pure RDP.

Useful information can be obtained by comparing our measured Brillouin frequencies ω_B to what we defined earlier as the uncoupled phonon frequencies ω_a (Equation (3-30)). The latter can be related to ω_B through the inverse coupling coefficient Q via Equation (3-37). Q can be obtained from the dielectric measurements. At high temperatures (above 200 K) the polarization coupling is small and nearly constant. Hence, Q is relatively constant at these temperatures.

Using the dielectric and Brillouin experiment results from Reference 7 for the concentrations x=0.25 and x=0.72, we were able to interpolate good estimates for the room temperature values of Q for the concentrations x=0.28 and x=0.42. The interpolated values for Q^{-1} are as follows,

$$Q^{-1}(0.28) = 0.0057 \qquad (5\text{-}1a)$$

$$Q^{-1}(0.42) = 0.0108 \qquad (5\text{-}1b)$$

The corresponding values of Q were then inserted in Equation (3-37) and the bare phonon frequencies ω_a were obtained

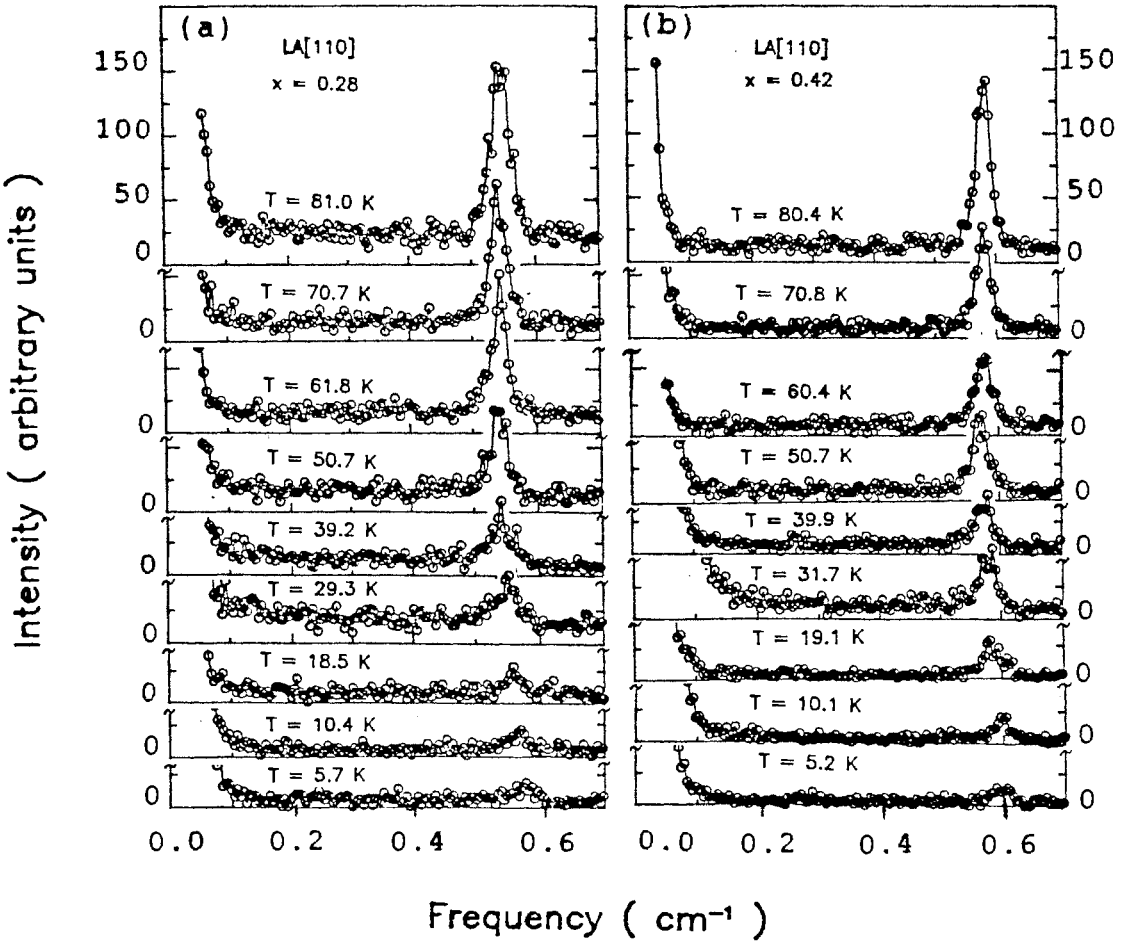

Figure 13. Antistokes Component of the LA[110] Acoustic Phonon as It Undergoes a Softening Around 50 K for (a) x=0.28 and (b) x=0.42. The Circles Are the Actual Measured Data.

from ω_B. The uncoupled phonon frequencies are shown by the squares in Figures 12a and 12b.

We have also used Reference 7 to interpolated the Debye temperature for our concentrations and obtained the following,

$$\theta(0.28) = 409 \text{ K} \quad (5\text{-}2a)$$
$$\theta(0.42) = 427 \text{ K} \quad (5\text{-}2b)$$

Next we used a linear regression fit of the calculated high temperature bare phonon frequencies to the Debye curve given by Equation (3-31) using the above results. From the fitting we obtained an extrapolation of the bare phonon frequency at T=0 K and the coefficient A representing a weighting factor for the amount of anharmonicity.

We found slightly different values of A for the two concentrations of interest. These values are

$$A(0.28) = 3.59\ 10^{-4} \quad (5\text{-}3a)$$
$$A(0.42) = 3.86\ 10^{-4} \quad (5\text{-}3b)$$

The above result for x=0.28 is in good agreement with Reference 7 where A was taken as a constant equal to $3.42\ 10^{-4}$. But for x=0.42 the difference is rather large and cannot be accounted for by the experimental uncertainties alone. We believe that the amount of anharmonicity expressed through the constant A increases slightly with higher concentrations. However these speculations cannot be confirmed until further complimentary experiments are performed, especially the dielectric and birefringence measurements.

A plot of the obtained Debye curve (Equation (3-31)) is

shown as a solid line in Figures 12a and 12b. At very low temperatures ω_B (open circles) tends towards ω_a but never reaches it. This suggests[8] that the phonon coupling to the polarization is not only due to linear polarization fluctuations ,which vanish at T=0 K, but also to electrostriction. We can then claim that at T=0 K, $\Delta\omega=\omega_a-\omega_B$ is mainly due to frozen polarization fluctuations associated with an Edwards-Anderson order parameter (Equation (3-40)) similar to a glass. This is consistent with the theoretical discussion of the latter part of Chapter III.

Finally, by comparing Figures 12a and 12b we can see clearly that $\Delta\omega(T=0)$ is larger for x=0.42 than for x=0.28. From this we conclude that the electrostriction coupling must increase with increased NH_4 concentration. In addition, we note that the depth of the minima around 50 K (i.e. $\Delta\omega$ at $T\approx50$ K) is about the same for both concentrations. This is all in good agreements with the previous study for x=0.25 and x=0.72 in Reference 8.

CHAPTER VI

CONCLUSIONS

This work was mainly directed towards a study of the temperature dependence of the LA[110] acoustic phonon using the Brillouin scattering technique. The two RADP samples studied were grown in our laboratory and have the following ammonium concentrations: x=0.28 and x=0.42.

At first several room temperature experiments were conducted on the above samples as well as on other crystals with concentrations x=0, 0.48 and 1. From the obtained spectra, the effective elastic constants were calculated and revealed a linear dependence on the concentration x. This result was not investigated further as it was not the objective of the present work and is left for future investigations.

From the temperature dependent experiments it was found that the LA[110] phonon undergoes some softening around 100°K then it starts hardening again below 50°K.
We have shown that this was due to both a linear and a quadratic coupling of this acoustic mode to the polarization fluctuations. The quadratic coupling to the polarization was made possible by the large electrostriction of these materials. We have found that at low temperature

electrostriction becomes the dominant mechanism and that it must increase with increased ammonium concentration. This is related to the frustration of the NH_4^+ ions which already started freezing below 100°K. The system then develops slow and almost static polarization fluctuations that can be described by an Edwards-Anderson order parameter similar to a glass. Our results were then compared to the ones for x=0.25, 0.35 and 0.72 in References 7 and 8 and the agreement was very satisfactory.

The RADP structural glasses are a family of materials that have emerged very recently (1982). Their transparency in the visible and ease of growth makes them good candidates for a variety of experiments. Among the experiments that would complement this work are the birefringence and the dielectric measurements. These studies will allow the measurements of some of the parameters needed for the fitting of the data namely the Debye temperature θ and the coupling constant Q respectively. In addition, plans are already underway for conducting several Raman scattering experiments on these samples. Further more, several nonlinear laser light scattering experiments are soon going to be performed on these materials. The purpose of these experiments is to investigate the potential applications of these materials in laser fusion and second harmonic generation similar to KDP.

REFERENCES

1. F. Jona and G. Shirane, Ferroelectric Crystals (MacMillan, New York, 1962), pp. 63-107.

2. J. P. Wicksted and R. C. Powell, Proposal,1987 (Unpublished).

3. M. E. Lines and A. M. Glass, Principles and Applications of Ferroelectrics and Related Materials (Claredon, Oxford, 1977).

4. E. Courtens, J. Phys. (Paris) Lett. 43, L199 (1982).

5. E. Courtens, Jpn. J. Appl. Phys. 24, Supp. 24-2, 70 (1985).

6. J. Slak, R. Kind, R. Blinc, E. Courtens and S. Zume, Phys. Rev. B 30, 85 (1984).

7. E. Courtens, R. Vacher and Y. Dagorn, Phys. Rev. B 33, 7625 (1986).

8. E. Courtens, R. Vacher and Y. Dagorn, Phys. Rev. B 36, 318 (1987).

9. S. F. Edwards and P. W. Anderson, J. Phys. F 5, 965 (1975).

10. R. M. Hooper, B. J. McArdle, R. S. Narang, and J. N. Sherwood in: Crystal Growth, 2nd ed., edited by B. R. Pamplin (Pergamon, New York, 1980), pp. 395-420.

11. G. M. Loiacono, Ferr., 71, 49 (1987).

12. Landolt-Börnstein, New Series Group III, 11, Elastic, Piezoelectric and Related Constants of Crystals, (Springer-Verlag, Berlin, 1966), pp. 56-59.

13. Fisher Scientic (Fair Lawn, New Jersey 07410).

14. Johnson Matthey Aesar Group (892 Lafayette Rd., P. O. Box 1087, Seabrook, NH03874).

15. L. Brillouin, Ann. Physik (Germany), 17, 88 (1922).

16. T. H. Maiman, Phys. Rev. Lett. 4, 564 (1960).

17. C. Kittel, Introduction to Solid State Physics, 5th ed. (Wiley, New York, 1976), pp. 111-116.

18. J. F. Nye, Physical Properties of Crystals, (Clarendon, Oxford, 1981).

19. H. Z. Cummins and P. E. Schoen in: Laser Handbook, Vol. 2 edited by Arecchi and Schultz-Dubois (North-Holland, Amsterdam, 1972), pp. 1029-1075.

20. W. Hayes, R. Loudon, Scattering of Light by Crystals, (Wiley, New York, 1978).

21. E. Courtens, Phys. Rev. Lett. 52, 69 (1984).

22. E. Courtens, Phys. Rev. Lett. 41, 1171 (1978).

23. E. Courtens and R. Gammon, Phys. Rev. B 24, 3890 (1981).

24. K. Fossheim and J. O. Fossum, in: Multicritical Phenomena, Vol. 106 of NATO ASI Series B: Physics, edited by R. Pynn and A. T. Skjeltorp (Plenum, New York, 1983), pp. 113-128.

25. E. Courten, F. Huard and R. Vacher Phys. Rev. Lett. 55, 722 (1985).

26. L. D. Landau and I. M. Khalatnikov, Dokl. Akad. Nauk SSSR 96, 469 (1954).

27. G. H. Gangwere, Ph. D. thesis, Oklahoma State University, Stillwater, 1989 (Unpublished).

28. E. M. Brody and H. Z. Cummins, Phys. Rev. B 9, 179, (1974).

29. A. R. King, I. B. Ferreira, V. Jaccarino and D. P. Belanger, Phys. Rev. B 37, 219 (1988).

30. D. J. Huskins, Quality Measuring Instruments in On-Line Process Analysis (Wiley, New York, 1982), pp. 47-48.

31. Janis Research Company, Inc. (2 Jewel Drive, Box 696 Wilmington, MA 01887-0896)

APPENDICES

APPENDIX A

TEMPERATURE MEASUREMENTS TECHNIQUE

This appendix is a detailed description of the temperature control and setup used in our Brillouin experiments. We will start by describing the He-Dewar and its operation then describe the sample holder and its special design.

The Janis He-Dewar is a very fine piece of equipment used for low temperature studies, especially light scattering experiments. A schematic of this dewar along with a brief description of its parts is shown in Figure 14. We will describe a detailed procedure that we followed when setting up the He-dewar for an experiment.

First the vacuum jacket is pumped to about 10 to 15 microns. Next the vacuum valve G is closed and the pump is moved to the valve on the helium vapor vent R and allowed to pump all the air from the sample tube. Then we open the needle valve I from F and allow pumping of the helium container. The pump was then isolated by closing the valve R and the helium container was back filled with helium gas. The last step consisted of pumping and refilling the helium container and sample tube several times to insure that only a helium environment existed in both. The needle

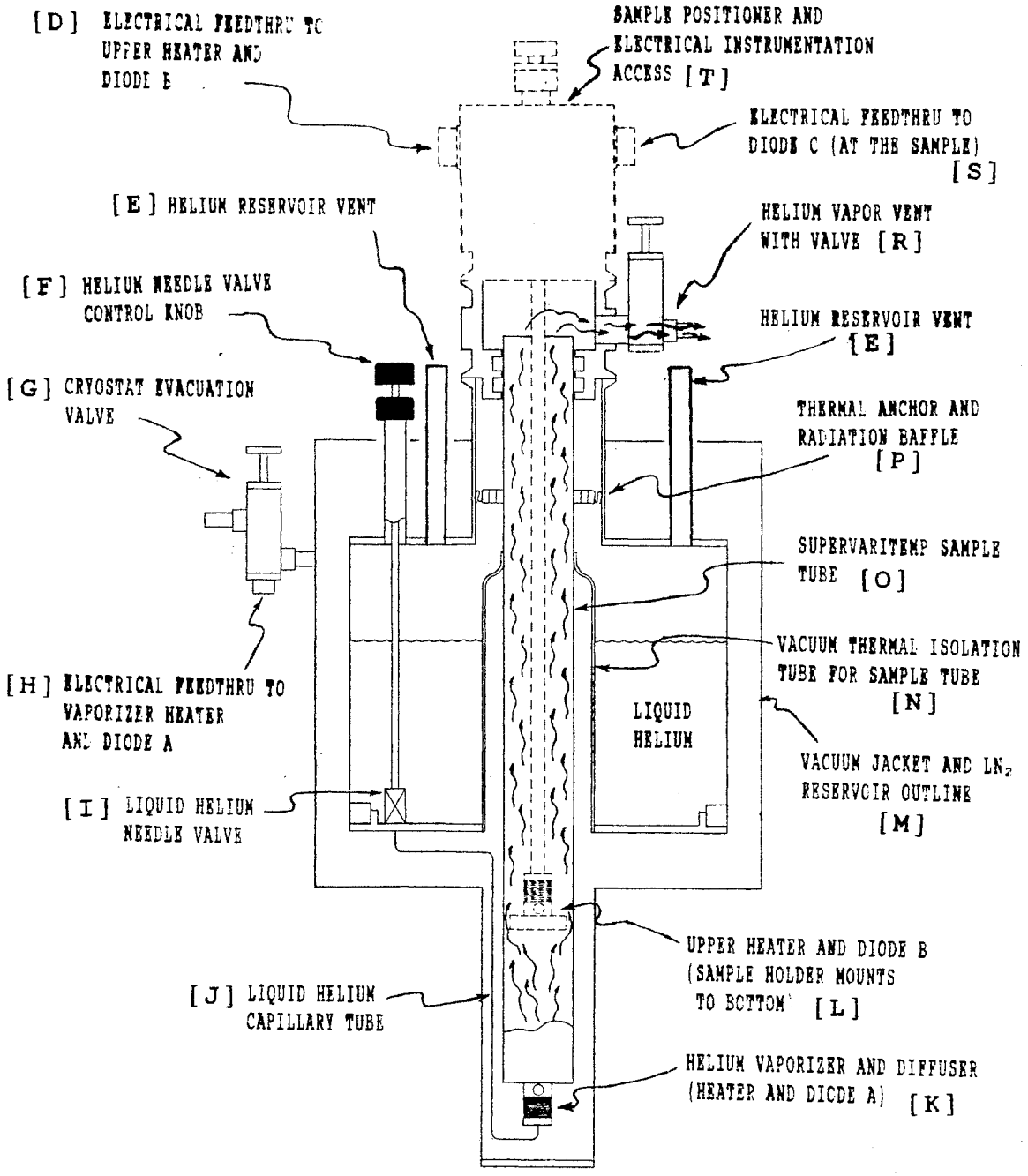

Figure 14. Schematics of Janis Model 8DT He-Dewar (from Reference 31)

valve is then closed and we are ready to start precooling the dewar by filling up the liquid-N_2 (LN_2) jacket. The precooling is a rather slow process (takes 8 to 10 hours) since the helium jacket is only cooled by radiation. For convenience the dewar is always left cooling over night. The next day we proceed with our preparation and back fill the He-jacket with helium gas. We also insure that the helium transfer line is free of air by running helium gas through it. Now we are ready to transfer liquid-He (LHe). We start first by inserting the He-transfer line all the way to the bottom of the He-jacket through one of the vents E while the other end of the transfer line is inserted into the liquid-He storage dewar. The latter was then pressurized to about 3 to 4 psi. The other He-jacket vent R was opened and a dry measuring rod was introduced through it to determine the amount of LHe accumulated. We usually transferred about 5 to 6 liters at a time. This would allow between 5 to 9 hours of temperature measurements depending on the temperature range at which we were operating the dewar and the LHe flow rate (needle valve opening).

The original hookups of the dewar to the Lake Shore temperature controller were such that the standard Si-diode located at the vaporizer assembly was connected to port A on the temperature controller. This input was matched to a standard curve that can accommodate any DT-470-SD type Si-diode. The other Si-diode was located

between the heater and the sample mount. This diode was calibrated by the Lake Shore Inc. according to the National Bureau of Standards specifications and a calibration curve was stored in the temperature controller to match input B.

The problem with the original setup was that the calibrated diode was kept closer to the upper heater for better stabilization of the temperature but it was already too far from the sample and, thus, could not detect the true sample temperature.

Our idea was to add another standard Si-diode sensor to the current setting. This sensor will be used to control the temperature using the upper heater. A schematic of the sample mount with the sample and diode in place is shown in Figure 15. The calibrated diode was mounted on one side of a 0.2mm thick copper plate S1 while the sample was mounted on the other. The rod S2 sticking out behind the sample was soldered to the plate S1 and the diode C was mounted on it. Diode C is then allowed to slide on three small pieces of teflon mounted on the inside of a hole through the sample holder. The teflon pieces act both to reduce the friction and isolate the diode from a direct heat flow from the sample mount. The freedom of diode C to move along its axis acts as a strain relief for the sample which is held against a copper frame S4. This design had solved the problem of cracking the sample due to large temperature changes.

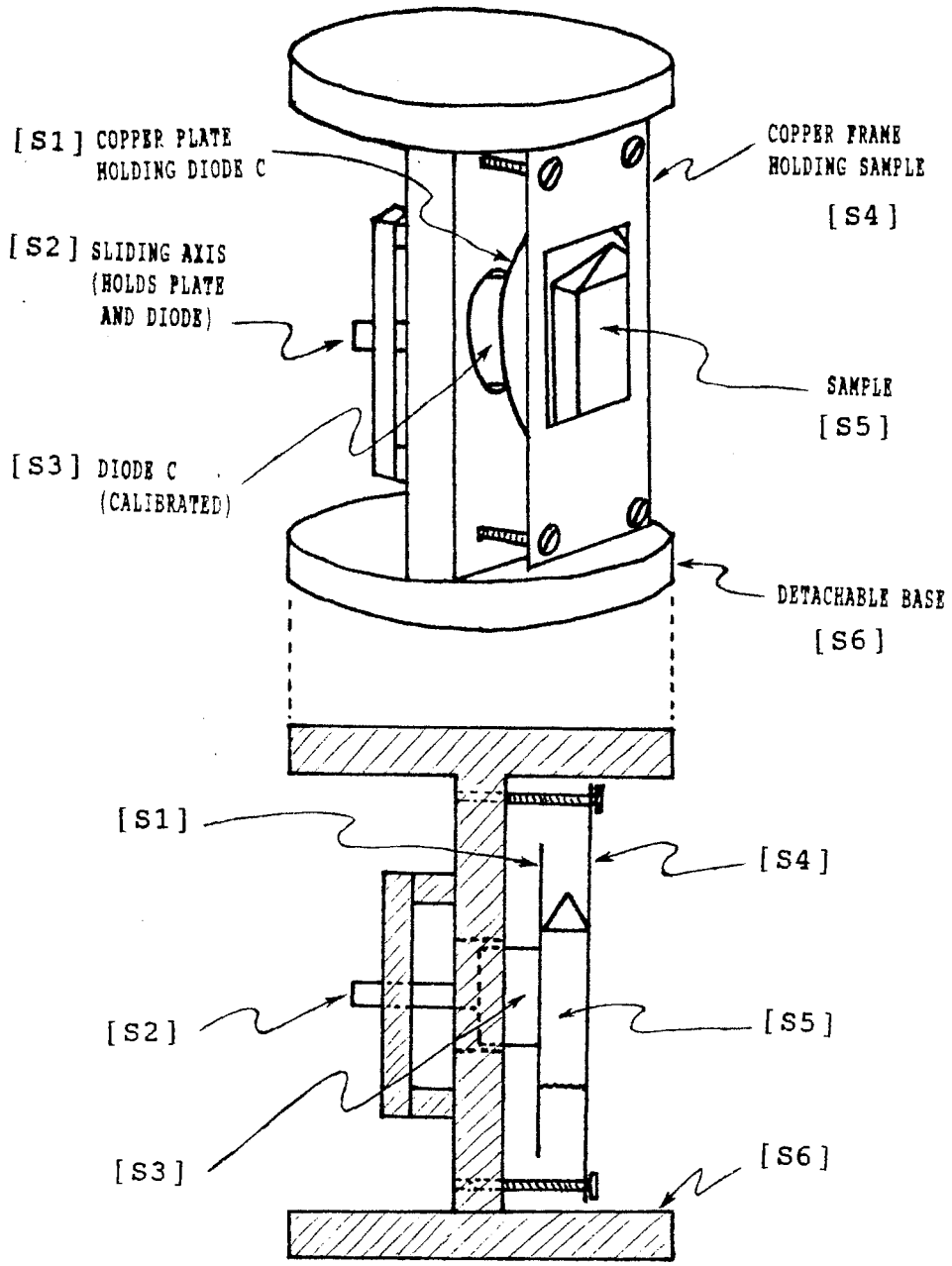

Figure 15. Schematics of the Sample Mount with the Si-Diode Sensor Mounted to It (See Text for Explanations)

With the new set up we have noticed during the course of our experiments that readings of up to about 5°K difference were observed between diodes B and C.

After the modifications were made the calibrated diode (C) is now connected to the calibrated input (input B) on the temperature controller at all times. When the temperature is controlled at the vaporizer heater diode A is connected to the standard input A on the temperature controller and diode B is not needed. On the other hand when the temperature is controlled using the upper heater, the output of diode B is read through the standard input A while both diode A and C are connected to the calibrated input B through a switch. This arrangement allows us to switch back and forth from A to C and read the exact temperature of the sample using diode C or check the cryogen accumulation at the vaporizer assembly by reading the input from diode A.

On the other hand, the He-dewar was also operated successfully with LN_2. This is done by filling up both the nitrogen and the helium jacket with LN_2. We must note here that the vaporizer heater (A) must not be used when the dewar is operating with LN_2 since the latter may not provide adequate cooling for the heater and would cause it to burn out.

A small modification had to be made to the sample holder due to the low boil off of the LN_2. This is done by replacing the detachable base S6 of the sample holder

shown in Figure 15 with a longer one (about 4 times longer than the one normally used with LHe). In this design the sample holder is much closer to LN_2 surface and could dissipate more heat from the upper heater allowing more evaporation of LN_2 and faster equilibration of the sample temperature. With this arrangement we were able to stabilize the temperature to within a few percent of the set point. Temperatures down to about 80°K were easily obtained.

The first major advantage of using LN_2 is that it does not require the over night cooling of the dewar and therefore an experiment can be started within an hour of preparation. The second major advantage of using LN_2 is that it would last more than 36 hours per filling. This is due to the fact that the LN_2 in the He-jacket is only surrounded by vacuum and LN_2 again so that hardly any of it is lost before being used in the sample tube. Finally, as we all know LN_2 is readily available and costs about 10 times less than LHe.

APPENDIX B

CONCENTRATION DETERMINATION

The purpose of this appendix is to present an explanation and support of the argument we used to determine the concentration of our RADP samples.

ADP and RDP crystals are isomorphs at room temperature with similar body centered tetragonal unit cells whose volumes are respectively τ_1=424.7 $Å^3$ and τ_2=422.3 $Å^3$. By comparing τ_1 and τ_2 we can see that the relative difference of the unit cell volumes is very small ($\frac{\Delta\tau}{\tau}\cong 0.006$). This is the main reason that RADP crystals can be obtained for the full range of concentrations.

It was shown by x-ray measurements[5] that RADP crystals are also isomorphs of their parents with similar body centered tetragonal unit cells whose volume τ has a magnitude that falls right between τ_1 and τ_2 for all ammonium concentrations. The changes of the unit cell volume as a function of concentration are very small so that the unit cell volume can be considered constant. In light of this reasonable approximation we can write the volume of an RADP sample as follows,

$$v = v_1 + v_2 \tag{B-1}$$

where v_1 and v_2 are respectively the equivalent volumes of ADP and RDP contained in the mixed sample. In the same manner we can write the mass of the RADP sample in the following form,

$$m = m_1 + m_2 \tag{B-2}$$

where m_1 and m_2 are respectively the masses of pure ADP and RDP contained in the mixed crystal. Using Equations (B-1) and (B-2), the density of the RADP sample is written as,

$$\rho = \frac{m}{v} = \frac{m_1 + m_2}{v_1 + v_2} \tag{B-3}$$

Expressing the volumes v_1 of ADP and v_2 of RDP in terms of the corresponding masses m_1 and m_2 and densities ρ_1 and ρ_2, Equation (B-3) becomes,

$$\rho = \frac{m_1 + m_2}{\frac{m_1}{\rho_1} + \frac{m_2}{\rho_2}} \tag{B-4}$$

Solving Equation (B-4) for $\frac{m_1}{m_2}$ we get

$$\frac{m_1}{m_2} = -\left(\frac{1-\frac{\rho}{\rho_2}}{1-\frac{\rho}{\rho_1}} \right) \tag{B-5}$$

Equation (B-5) is the expression we used (Equation (4-7)) to determine the ammonium concentration of our RADP samples as shown in Chapter 4.

VITA

ABDELLATIF BOUCHALKHA

Candidate for the Degree of

Master of Science

Thesis: TEMPERATURE DEPENDENCE OF THE LA[110] BRILLOUIN SHIFT IN THE STRUCTURAL GLASS : $Rb_{1-x}(NH_4)_xH_2PO_4$

Major Field: Physics

Biographical:

Personal Data: Born in Marrakech, Morocco, January 1, 1962, the son of Boujemaa and Fatna Bouchalkha.

Education: Graduated from Abou El Abbas Essebti High School, Marrakech, Morocco, in May, 1980; received Bachelor of Science degree from Central State University, Edmond, Oklahoma, in May, 1986, with a major in Physics and a minor in Mathematics; completed the requirements for the Master of Science degree at Oklahoma State University in July, 1989.

Professional Experience: Undergraduate Research Assistant, Central State University, Edmond, Oklahoma, August 1985 to May 1986; Teaching Assistant, Department of Physics, Oklahoma State University, August, 1986 to May, 1987; Graduate Research Assistant, June, 1987 to present. Member of the American Physical Society, and Sigma Pi.